Lagrangian Measurement of Steep Directionally Spread Ocean Waves: Second-Order Motion of a Wave-Following Measurement Buoy

M. L. McAllister* and T. S. van den Bremer

Department of Engineering Science, University of Oxford, Parks Road, Oxford OX1 3PJ, UK

Corresponding author address: Department of Engineering Science, University of Oxford, Parks Road, Oxford OX1 3PJ, UK.

E-mail: mark.mcallister@eng.ox.ac.uk

ABSTRACT

The notion that wave-following buoys provide less accurate measurements of extreme waves than their Eulerian counterparts is a perception commonly held by oceanographers and engineers (Forristall 2000, J. Phys. Oceanogr., **30**, 1931-1943). By performing a direct comparison between the two types of measurement under laboratory conditions, we examine one of the hypotheses underlying this perception and establish whether wave measurement buoys in extreme ocean waves correctly follow steep crests and behave in a purely Lagrangian manner. We present a direct comparison between Eulerian gauge and Lagrangian buoy measurements of steep directionally spread and crossing wave groups on deep water. Our experimental measurements are compared to exact (Herbers and Janssen 2016, J. Phys. Oceanogr., **46**, 1009-1021) and new approximate expression for Lagrangian second-order theory derived herein. We derive simple closed-form expressions for the second-order contribution to crest height representative of extreme ocean waves, namely for a single narrowly spread wave group, two narrowly spread crossing wave groups, and a strongly spread single wave group. In the limit of large spreading or head-on crossing, Eulerian and Lagrangian measurements become equivalent. For the range of conditions we test, we find that our buoy behaves in a Lagrangian manner, and our experimental observations compare extremely well with predictions made using second-order theory. Generally, Eulerian and Lagrangian measurements of crest height are not significantly different for all degrees of directional spreading and crossing. However, second-order bound-wave energy is redistributed from super-harmonics in Eulerian measurements to sub-harmonics in Lagrangian measurement, which affects the 'apparent' steepness inferred from time histories and poses a potential issue for wave buoys that measure acceleration.

1. Introduction

Wave-following buoys are commonly used as devices to measure free surface elevation in the oceans. This is, in part, owing to their relative ease of installation; unlike the majority of Eulerian measurement devices, buoys do not require a supporting structure. Measurements made with both buoys and Eulerian devices are used in operational oceanography and ocean engineering in various forms. Summary statistics such as significant wave height H_s and peak period T_p are commonly used to calibrate phase-averaged ocean forecast and hindcast models (Janssen et al. 1997; Bidlot et al. 2002) and to characterise environmental conditions across the oceans (Hasselmann et al. 1980; Pontes 1998; Mork et al. 2010; Fedele and Arena 2010; Lenee-Bluhm et al. 2011). Time-domain measurements are used to investigate wave dynamics and to gain insight into processes such as wave breaking and freak wave formation (Holthuijsen and Herbers 1986; Soares et al. 2004; Waseda et al. 2014; Whittaker et al. 2016). In such studies, the two types of measurement are often used interchangeably.

However, within the oceanographic and ocean engineering communities, it is generally perceived that wave buoys are less accurate, particularly when concerning the measurement of extreme waves (Allender et al. 1989; Forristall 2000; Dysthe and Müller 2008; Collins III et al. 2014). Various explanations are offered for this perceived inaccuracy, such as a lack of compliance in the mooring configuration or the ability of a buoy to move horizontally causing it avoid the highest crests (Allender et al. 1989; Krogstad and Barstow 2000), the cancellation of second-order super-harmonic contributions to crest height owing to their Lagrangian motion (Longuet-Higgins 1986; Rademakers 1993), and low sampling frequencies resulting in wave crests being missed (Forristall 2000). For completeness, we note the probability of observing extreme waves in single-

point observations (Eulerian or Lagrangian) is different from spatial-temporal observations (e.g. Benetazzo et al. 2017), although we do not focus on this herein.

In principle, a floating wave-following buoy measures the Lagrangian free surface elevation $\eta_{\mathrm{L}}(\mathbf{x}_{\mathrm{H}}(t),t)$, which is function of time t both directly and indirectly through its dependence on its time-varying horizontal position $\mathbf{x}_{\mathrm{H}}(t)$, unlike a Eulerian measurement $\eta_{\mathrm{E}}(\mathbf{x}_{\mathrm{H},0},t)$, which is made at a fixed location $\mathbf{x}_{\mathrm{H},0}$. In the limit in which waves are of small amplitude and their behaviour is approximated well by linear theory, Lagrangian and Eulerian measurements are identical. The nonlinearity associated with steep waves can cause the two types of measurement to differ.

Longuet-Higgins (1986) examined this for regular progressive waves on deep water, showing how measurements may differ owing to nonlinear effects that occur at second-order in amplitude. The horizontal motion of a Lagrangian observer serves to cancel out the sharpening of crests and broadening of troughs, observed in a Eulerian frame of reference that is a result of second-order super-harmonic wave components. This also results in an increase in the position of the mean free surface in Lagrangian measurements by approximately $a^2k/2$, when compared to a Eulerian measurement, where a is the amplitude of a wave, $k = 2\pi/\lambda$ is its wavenumber, and λ its wavelength (Longuet-Higgins 1986). Additionally, the Stokes drift velocity u_{S} causes a Doppler shift of the wave speed c (in the Eulerian reference frame), and the measured wave period in the Lagrangian reference frame T_{L} increases compared to the period in the Eulerian reference frame T_{E} (Longuet-Higgins 1986),

$$\frac{T_{\mathrm{L}} - T_{\mathrm{E}}}{T_{\mathrm{E}}} = \frac{u_{\mathrm{S}}}{c - u_{\mathrm{S}}}, \tag{1}$$

which has recently been studied experimentally by Grue and Kolaas (2019) for finite depth.

Following on from Srokosz and Longuet-Higgins (1986), Herbers and Janssen (2016, henceforth HJ16) investigated how second-order effects apply to irregular waves on finite depth by extending existing Eulerian multi-component second-order theory (see Hasselmann 1962; Longuet-Higgins

and Stewart 1962; Sharma and Dean 1981; Dalzell 1999) to a Lagrangian reference frame through the inclusion of an additional term to account for horizontal motion of surface-following particle. HJ16 illustrated that for irregular waves on deep water, much like regular waves, the position of the 'mean' or 'wave-averaged' free surface (sub-harmonic bound-wave components at second order) is shifted up. Where a 'set-down' (negative depression) is observed in a Eulerian measurement of a wave group, a 'set-up' (positive hump) is observed in the corresponding Lagrangian measurement. Similarly, as for a regular wave, super-harmonic components disappear in a Lagrangian measurement. HJ16 note that for waves on shallow water, the Eulerian sub-harmonic second-order bound wave components approach resonance and are strongly amplified, dominating over the Lagrangian components, which are not amplified by water depth in the same way. Thus, Lagrangian measurements in shallow water are approximately equal to their Eulerian equivalents.

A number of studies have considered the contribution that second-order nonlinearity makes to the crest height of extreme waves in a Eulerian frame of reference, finding that the local directional conditions have a strong effect. For steep wave groups in unidirectional and weakly spread conditions, bound second-order sub-harmonic or 'difference' waves form a depression in the wave-averaged surface elevation often referred to as a set-down (Longuet-Higgins and Stewart 1962). In the case of crossing and strongly directionally spread wave systems, the set-down of sub-harmonic bound waves underneath a wave group can turn into a set-up, enhancing the maximum crest amplitude, as theoretically predicted (Okihiro et al. 1992; Herbers et al. 1994; Toffoli et al. 2006; Christou et al. 2009) based on second-order interaction kernels (Hasselmann 1962; Sharma and Dean 1981; Dalzell 1999; Forristall 2000), observed in field data (Santo et al. 2013; Walker et al. 2004; Toffoli et al. 2007) and recently in detailed laboratory experiments (McAllister et al. 2018).

Wave measurement buoys are positively buoyant and float partially submerged on the water surface. Datawell's Waverider buoy and other simple spherical buoys operate approximately half

submerged and typically have densities in the range $0.55 - 0.66\rho_w$, where ρ_w is the density of sea water. As these buoys are neither neutrally buoyant nor completely submerged, they will not necessarily behave in a purely Lagrangian manner. In different physical contexts, enhanced Stokes drift has been predicted due to the particle's inertia for very small submerged particles (Santamaria et al. 2013), due to the particle sliding down the slope for floating plates (Meylan et al. 2015) and due to wave breaking (Pizzo et al. 2019). Additionally, wave measurement buoys are often moored (to the seabed); the force provided by a mooring system may also cause buoy motion to deviate from purely Lagrangian.

In practice, measurement buoys can be deployed without a mooring, but are most commonly moored. Measurement buoy moorings are designed to have minimal effect on their motion; the resulting designs are complex and vary significantly depending on the depth of water they are installed in. Their general design comprises a slack buoyant inflexible section connected to the seabed, which allows for a large range of lateral motion. From this, a section composed of a flexible material then connects to the buoy itself. The flexibility of this second section reduces its effect on the heave motion of the buoy.

Short of side-by-side comparison, it is difficult to establish to what extent a buoy will behave in a true Lagrangian manner in the ocean and how its measurements will compare to measurements of the Eulerian free surface elevation at the same location. Various studies have made comparisons of in-situ measurements between various buoy designs (Allender et al. 1989; O'Reilly et al. 1996; Ashton and Johanning 2015; Raghukumar et al. 2019) and with other types of sensors (O'Reilly et al. 1996; Forristall et al. 2004; Herbers et al. 2012). Liu et al. (2015) carried out experiments to investigate the performance of slack-moored disc-type wave buoys, which they compared to nearby gauge measurements, finding good agreement when considering the spectral parameters significant wave height and peak period.

To the authors' knowledge, there are no studies that make a direct comparison between Eulerian and Lagrangian wave-following measurement devices and that focus on second-order aspects of the motion. In this paper, we perform a series of laboratory experiments with a scaled model buoy to make exactly this comparison and thus provide experimental validation of the Lagrangian second-order theory of HJ16. Using the multiple-scales method, we derive new narrow-banded approximations to the multi-chromatic theory of HJ16 for three cases: a single weakly directionally spread wave group, two crossing weakly directionally spread wave groups and a single strongly directionally spread wave group. The resulting expressions are simple and allow a direct appreciation of the magnitude of the second-order sub- and super-harmonic bound waves, as well as their physical origins in different cases.

In carrying out our experiments, we set out to (partially) answer the question whether wave-following buoys (without mooring) behave in a purely Lagrangian manner. In particular, we consider the behaviour of scaled spherical model buoys in steep directionally spread and crossing wave groups on deep water. We focus on wave groups, as they provide a good approximation of the shape of extreme waves in the ocean (Lindgren 1970; Boccotti 1983; Phillips et al. 1993; Santo et al. 2013; Gemmrich and Thomson 2017).

This paper is laid out as follows. First, in §2, we review and compare existing Eulerian and Lagrangian second-order theory, and present our novel approximate second-order expressions derived for waves groups. We then give details of our experimental method in §3, and present our results in §4. Finally, we discuss the generality of our findings and draw conclusion in §5.

2. Second-order theory

In this section, we introduce existing Eulerian and Lagrangian multi-chromatic second-order theory (§2.b). We then present our new narrow-banded approximations, derived using the multiple-

scales method, for three cases: a single weakly directionally spread wave group (WSG) (§2.c), two crossing wave groups (CGs) (§2.d), and a single strongly directionally spread wave group (SSG) (§2.e). We also evaluate the Stokes drift velocity and the resulting change in the Lagrangian frequency for each of these three cases. Motivated by ocean applications, we focus on cases where the water is deep relative to the wavelength of the carrier wave (i.e. $k_0 d \gg 1$ with $k_0 = 2\pi/\lambda_0$ the carrier wavenumber and d depth).

a. Governing equations

We assume a three-dimensional body of water of depth d and indefinite lateral extent with a coordinate system (x,y,z), where x and y denote the horizontal coordinates, and z the vertical coordinate measured from the undisturbed water level upwards. Inviscid, incompressible and irrotational flow is assumed and, as a result, the velocity vector can be defined as the gradient of the velocity potential, $\mathbf{u} = \boldsymbol{\nabla}\phi$, and the governing equation within the domain of the fluid is Laplace,

$$\nabla^2\phi = 0 \quad \text{for } -d \le z \le \eta(x,y,t), \tag{2}$$

where $\eta(x,y,t)$ denotes the free surface. The kinematic and dynamic free surface boundary conditions at $z = \eta(x,y,t)$ are, respectively,

$$w - \frac{\partial\eta}{\partial t} - u\frac{\partial\eta}{\partial x} - v\frac{\partial\eta}{\partial y} = 0, \quad g\eta + \frac{\partial\phi}{\partial t} + \frac{1}{2}|\nabla\phi|^2 = 0, \tag{3a,b}$$

where gravity g acts in the negative z direction and $|\nabla\phi|^2 = u^2 + v^2 + w^2$. Finally, there is a no-flow bottom boundary condition requiring that $\partial\phi/\partial z = 0$ at $z = -d$. By retaining terms up to quadratic in the amplitude of the waves, the two free surface boundary conditions in (3) can be combined into two forcing equations for the second-order potential and free surface, respectively (e.g. Longuet-Higgins and Stewart (1964); McAllister et al. (2018)):

$$\left(\frac{\partial}{\partial z} + \frac{1}{g}\frac{\partial^2}{\partial t^2}\right)\phi_{\mathrm{E}}^{(2)}\bigg|_{z=0} = \nabla_{\mathrm{H}} \cdot \left(\mathbf{u}_{\mathrm{H}}^{(1)}\eta^{(1)}\right)\bigg|_{z=0} \tag{4}$$

$$-\frac{1}{g}\frac{\partial}{\partial t}\Big(\frac{\partial^2\phi^{(1)}}{\partial z\partial t}\eta^{(1)}+\frac{1}{2}|\nabla\phi|^2\Big)\Big|_{z=0},$$

$$\eta^{(2)}_{\mathrm{E}}=\frac{-1}{g}\left(\frac{\partial\phi^{(2)}_{\mathrm{E}}}{\partial t}+\Big(\frac{\partial^2\phi^{(1)}}{\partial z\partial t}\eta^{(1)}+\frac{1}{2}|\nabla\phi|^2\Big)\right)\Bigg|_{z=0}, \tag{5}$$

where the superscripts denote the order in amplitude and we use (superfluous) subscripts E to denote Eulerian in order for distinction with Lagrangian (L) to be made below (n.b. we only introduce these subscripts for second-order quantities). For simplicity, we will refer to fields or quantities recorded by a Lagrangian observer as Lagrangian, e.g. Lagrangian free surface η_{L} and Lagrangian frequency ω_{L}. The subscript H denotes horizontal components only, so that $\mathbf{u}_{\mathrm{H}}=(u,v,0)$.

b. Multi-component second-order theory (review)

Assuming independence between the directional $\Omega(\theta)$ and amplitude $\hat{\eta}(\omega)$ distributions, the linear free surface can be given by a summation over N_k discrete components in N_θ directions:

$$\eta^{(1)}(\mathbf{x},t)=\sum_{n=1}^{N_k}\sum_{i=1}^{N_\theta}\Omega(\theta_i)\hat{\eta}_n\cos(\varphi_{n,i})\delta k\delta\theta, \tag{6}$$

where $\varphi_{n,i}=\mathbf{k}_{n,i}\cdot\mathbf{x}_{\mathrm{H}}-\omega_n t+\mu_{n,i}$ and the wavenumber vector $\mathbf{k}_{n,i}=k_n\big(\cos(\theta_i),\sin(\theta_i)\big)$ has magnitude k_n, and θ is measured anti-clockwise from the positive x-axis. Frequencies and wavenumbers are related by the linear dispersion relationship $\omega_n=\sqrt{g|\mathbf{k}_n|\tanh(|\mathbf{k}_n|d)}$. Similarly, the linear potential is,

$$\phi^{(1)}(\mathbf{x},t)=\sum_{n=1}^{N_k}\sum_{i=1}^{N_\theta}\frac{\omega_n}{|\mathbf{k}_n|}\Omega(\theta_i)\hat{\eta}_n e^{|\mathbf{k}_n|z}\sin(\varphi_{n,i})\delta k\delta\theta. \tag{7}$$

Evaluating (4) and (5) using these linear solutions results in the following expression for second-order free surface elevation,

$$\eta^{(2)}_{\pm}(\mathbf{x},t)=\sum_{n=1}^{N_k}\sum_{m=1}^{N_k}\sum_{i=1}^{N_\theta}\sum_{j=1}^{N_\theta}\hat{\eta}_n\hat{\eta}_m\Omega(\theta_i)\Omega(\theta_j)B^{\pm}_{m,n,i,j}\cos(\varphi_{n,i}\pm\varphi_{m,j})(\delta k)^2(\delta\theta)^2, \tag{8}$$

where the subscript $\pm$ denotes bound waves which occur as the sum $(+)$ or difference $(-)$ of the frequencies of their interacting parent waves, and $B^{\pm}$ represent the respective second-order interaction kernels. The structure of these second-order interaction kernels may be defined to account for Eulerian $B^{\pm}_{\mathrm{E}}$ (e.g. Dalzell (1999)) or Lagrangian $B^{\pm}_{\mathrm{L}}$ (Herbers and Janssen 2016) free surface motion.

Although expressions for the 'frequency-difference' terms in a multi-directional sea can be distilled from Hasselmann (1962) (cf. Okihiro et al. (1992)), Sharma and Dean (1981), Dalzell (1999) and Forristall (2000) are commonly credited for extending the work of Longuet-Higgins and Stewart (1962) to finite depth directional seas, allowing for interactions between-parent wave components of different frequencies and travelling in different directions (see Pellet et al. (2017) for a recent re-derivation that also includes pressure).

Restricting our attention to terms up to second-order in amplitude, the Eulerian and the Lagrangian free surface are related by:

$$\eta^{(2)}_{\mathrm{L}} = \eta^{(2)}_{\mathrm{E}} + \Delta\eta^{(2)}_{\mathrm{L}} \quad \text{with} \quad \Delta\eta^{(2)}_{\mathrm{L}} = \Delta\mathbf{x}^{(1)}_{\mathrm{H}} \cdot \boldsymbol{\nabla}_{\mathrm{H}}\eta^{(1)}, \tag{9}$$

where $\Delta\mathbf{x}^{(1)}_{\mathrm{H}}$ is the linear horizontal motion (i.e. $\partial\Delta\mathbf{x}^{(1)}_{\mathrm{H}}/\partial t = \mathbf{u}^{(1)}_{\mathrm{H}}$). Resulting expressions for the second-order interaction kernels for a Lagrangian observer were derived in a unidirectional framework by Srokosz and Longuet-Higgins (1986) and Prevosto et al. (2000) and, more recently, in fully directional seas by HJ16.

Distinguishing super- and sub-harmonic (or 'mean') terms, we will now consider the Eulerian and Lagrangian surface elevation when the spectrum is narrow banded for three cases: a single weakly directionally spread wave group (WSG) (§2.c), two crossing wave groups (CGs) (§2.d), and a single strongly directionally spread wave group (SSG) (§2.e). Our intention here is to develop an understanding of the behaviour at second-order that cannot be directly inferred from the

complicated kernels. In doing so, we derive simple expressions for the second-order Eulerian and Lagrangian free surface elevations and frequencies. To do so, we thus focus on narrow-banded spectra and derive results using the method of multiple scales, considering only leading-order terms.

In each case, we implement the following non-dimensionalisation: $\tilde{\eta}^{(2)} \equiv \eta^{(2)}/(k_0 a_0^2/2)$, where the notation $\tilde{\eta}^{(2)}$ also indicates that our expressions are evaluated at the point of focus ($x = 0$, $y = 0$), only the dependence on the fast time scale of of the linear waves is maintained, and $a_0 \equiv |A(t = 0, y = 0, t = 0)|$ is the focused linear amplitude of the surface elevation envelope A. We choose this point because the second-order surface elevations reach their extrema here. Results are summarized in table 1 and compared to exact multi-component second-order theory in §2.f.

c. A single weakly spread wave group (WSG)

If we consider a weakly directionally spread wave group (WSG) as a carrier wave with frequency ω_0 and wavenumber k_0, which is slowly modulated by the envelope $A(X,Y)$, we may express the linear free surface elevation and potential as,

$$\eta^{(1)} = A(X,Y)\cos(\varphi_0), \quad \phi^{(1)} = \frac{\omega_0}{k_0} A(X,Y) e^{k_0 z} \sin(\varphi_0), \tag{10a,b}$$

with $\varphi_0 = k_0 x - \omega_0 t + \mu_0$. We have assumed that the linear waves propagate on deep water ($k_0 d \gg 1$), so that the linear dispersion relation becomes $\omega_0^2 = g k_0$. The water depth is not truly infinite. In our experiments, the water depth is shallow to intermediate with respect to our wave group ($d/\sigma_x \ll 1$ or $d/\sigma_x = O(1)$, respectively). To leading-order in the multiple-scales parameter ε ($\varepsilon_x \equiv 1/(k_0\sigma_x) = O(\varepsilon)$ and $\varepsilon_y \equiv 1/(k_0\sigma_y) = O(\varepsilon)$ with σ_x and σ_y denoting the characteristic spatial scales of the group in its direction of propagation and the direction orthogonal to it, re-

spectively), the group is a function of the slow variables: $X \equiv \varepsilon_x\big(x - c_{g,0}t\big)$ and $Y \equiv \varepsilon_y y$, where $c_{g,0} = \mathrm{d}\omega_0/\mathrm{d}k_0 = \omega_0/(2k_0)$ is the group velocity.

1) Eulerian

From (5), it is clear that there are two contributions to the Eulerian second-order surface $\eta^{(2)}_{\mathrm{E}}$: from the (time derivative of the) second-order potential $\phi^{(2)}_{\mathrm{E}}$ and from a combination of first-order terms,

$$\eta^{(2)}_{\mathrm{E,LF}} \equiv \frac{-1}{g}\left(\frac{\partial^2\phi^{(1)}}{\partial z\partial t}\Big|_{z=0}\eta^{(1)} + \frac{1}{2}|\nabla\phi|^2\big|_{z=0}\right), \tag{11}$$

which we term the linear forcing term $\eta^{(2)}_{\mathrm{E,LF}}$. Its super-harmonic component can be obtained from substituting (10) into (11):

$$\eta^{(2)}_{\mathrm{E,LF},+} = \frac{k_0 A(X,Y)^2}{2}\cos(2\varphi_0), \tag{12}$$

and its sub-harmonic component is zero in deep-water ($k_0 d \gg 1$) unless waves cross (hence this sub-harmonic component was termed the crossing wave term in McAllister et al. (2018), i.e. $\eta_{\mathrm{E,CW}} \equiv \eta^{(2)}_{\mathrm{E,LF},-}$; see §2.d). We can thus ignore it in the case of a single weakly spread wave group. Substituting (10) into (4) and solving for $\phi^{(2)}_{\mathrm{E}}$ yields a leading-order expression for the Eulerian second-order potential,

$$\begin{aligned}\phi^{(2)}_{\mathrm{E}} = \frac{\imath\omega_0}{8\pi^2}\int_{-\infty}^{\infty}\int_{-\infty}^{\infty}\frac{\kappa\cosh\left(\sqrt{\kappa^2+\lambda^2}(z+d)\right)}{\sqrt{\kappa^2+\lambda^2}\sinh\left(\sqrt{\kappa^2+\lambda^2}d\right)}\\ \times\widehat{A^2}\exp\left(\imath(\kappa\tilde{x}+\lambda\tilde{y})\right)\mathrm{d}\kappa\mathrm{d}\lambda,\end{aligned} \tag{13}$$

where $\tilde{x} \equiv x - c_{g,0}t$, $\tilde{y} \equiv y$, and $\widehat{A^2}$ denotes the Fourier transform of the square of the packet. As is well known, the potential does not have a super-harmonic component ($\phi^{(2)}_{\mathrm{E}} = \phi^{(2)}_{\mathrm{E},-}$, e.g. Stokes (1847)). Equation (13) can then be substituted into (5) and combined with (12) to give the Eulerian

free surface elevation:

$$\eta_{\mathrm{E}}^{(2)} = \frac{-1}{16\pi^2} \int_{-\infty}^{\infty} \int_{-\infty}^{\infty} \frac{\kappa^2 \widehat{A^2} \exp\left(\imath(\kappa\tilde{x} + \lambda\tilde{y})\right)}{\sqrt{\kappa^2+\lambda^2}\tanh\left(\sqrt{\kappa^2+\lambda^2}d\right)} \mathrm{d}\kappa\mathrm{d}\lambda + \frac{k_0 A(X,Y)^2}{2}\cos(2\varphi_0). \tag{14}$$

If we further assume that depth is shallow with respect to the group scale ($d/\sigma_x \ll 1$), the double integral in (14) can be explicitly evaluated at $X = 0$, $Y = 0$ to give in non-dimensional form (i.e. $\tilde{\eta}^{(2)} \equiv \eta^{(2)}(X=0,Y=0)/(k_0 a_0^2/2)$) (McAllister et al. 2018):

$$\tilde{\eta}_{\mathrm{E}}^{(2)} = -\frac{1}{2k_0 d}\frac{1}{1+R} + \cos(2\varphi_0), \tag{15}$$

where $R = \sigma_x/\sigma_y$ is the aspect ratio of the group and a measure of directional spreading, with $R \to 0$ corresponding to unidirectional waves.

Equation (15) gives the familiar result for the second-order bound waves of a weakly directionally spread wave group. The slowly-varying part represents a set-down of the free surface, which diminishes as the amount of directional spreading R increases, noting that (15) is only valid for weak directional spreading. The rapidly-varying super-harmonics are unaffected by weak directional spreading and take the same form as for a unidirectional monochromatic wave. In fact, without loss of generality, the dependence of the super-harmonic term on the rapidly-varying $2\varphi_0$ with $\varphi_0 = k_0 x - \omega_0 t + \mu_0$ and on the slowly-varying envelope $A(X,Y)$ can be maintained. This is not true for the slowly-varying mean term representing a set-down, which can only be explicitly evaluated at the point and time of focus ($X = 0$, $Y = 0$) (McAllister et al. 2018).

2) Lagrangian

From (10), we can readily obtain the leading-order Lagrangian correction term to the second-order free surface elevation $\Delta\eta_L^{(2)}$, as defined in (9), which accounts for the horizontal motion a

Lagrangian observer:

$$\Delta\eta_{\mathrm{L}}^{(2)} = \frac{k_0 A(X,Y)^2}{2}\left(1-\cos(2\varphi_0)\right), \tag{16}$$

which comprises a mean set-up term and a super-harmonic term that is out of phase with its Eulerian super-harmonic counterpart in (14). Combining this with $\eta_{\mathrm{E}}^{(2)}$ in (15), we obtain in non-dimensional form:

$$\tilde{\eta}_{\mathrm{L}}^{(2)} = 1 - \frac{1}{2k_0 d}\frac{1}{1+R}. \tag{17}$$

For a single weakly spread wave group, the Lagrangian and the Eulerian super-harmonic terms exactly cancel each other out, as is well known (Longuet-Higgins 1986), leaving only mean terms, as predicted in Herbers and Janssen (2016). For a Lagrangian observer, these mean terms take the form of a set-up, which is only weakly diminished by the effect of the Eulerian set-down. The Lagrangian correction term $\Delta\eta_{\mathrm{L}}^{(2)}$ does not depend on depth d, whereas the Eulerian term depends inversely on depth d (and is small, noting that $k_0 d \gg 1$ here).

3) Stokes drift velocity and Lagrangian frequency

For a Lagrangian measurement device, the measured linear wave period is increased by a Doppler shift induced by Stokes drift (Longuet-Higgins 1986), which is generally given by:

$$\mathbf{u}_{\mathrm{S}} \equiv \overline{\Delta\mathbf{x}^{(1)} \cdot \boldsymbol{\nabla}\mathbf{u}^{(1)}}, \tag{18}$$

which is the product of the linear displacement vector $\Delta\mathbf{x}^{(1)}$ and the gradient of the linear velocity. For a single weakly spread wave group on deep water, the Stokes drift (18) only has a leading-order term in the x-direction (the direction of propagation of the carrier wave):

$$u_{\mathrm{S}} = k_0 \omega_0 A^2. \tag{19}$$

Using the Doppler shift $\omega_{\mathrm{L},0} = k_0(c_{p,0} - u_{\mathrm{S}})$ with $c_{p,0} = \omega_0/k_0$ the phase velocity, we obtain the Lagrangian frequency

$$\omega_{\mathrm{L},0} = \omega_0 \left(1 - k_0^2 A^2\right), \tag{20}$$

which is equivalent to the result by Longuet-Higgins (1986) for a unidirectional monochromatic wave (except for slow dependence of the envelope and an apparently superfluous $1/2$ in (2.4) of Longuet-Higgins (1986)), indicating that the presence of a group or (weak) directional spreading does not play a leading-order role.

d. Two crossing wave groups (CWGs)

If we now consider two crossing wave groups, with the first group travelling in the x-direction ($\theta_p = 0$) and the second travelling in the direction $\theta_p = \Delta\theta$, the linear free surface elevation and potential are, respectively,

$$\eta^{(1)} = A_1(X_1, Y_1)\cos(\varphi_1) + A_2(X_2, Y_2)\cos(\varphi_2), \tag{21}$$

$$\phi^{(1)} = \frac{\omega_0}{k_0} A_1(X_1, Y_1) e^{k_0 z}\sin(\varphi_1) + \frac{\omega_0}{k_0} A_2(X_2, Y_2) e^{k_0 z}\sin(\varphi_2), \tag{22}$$

with phases $\varphi_1 = k_0 x - \omega_0 t + \mu_1$ and $\varphi_2 = k_0 x\cos(\Delta\theta) + k_0 y\sin(\Delta\theta) - \omega_0 t + \mu_2$. Both groups have identical frequencies ω_0 and wavenumber magnitudes k_0, satisfying the deep-water linear dispersion relationship $\omega_0^2 = g k_0$. Group 1 is a function of the slow scales $X_1 = \varepsilon_x(x - c_{g,0}t)$ and $Y_1 = \varepsilon_y y$ and group 2 of $X_2 = \varepsilon_x(x\cos(\Delta\theta) + y\sin(\Delta\theta) - c_{g,0}t)$ and $Y_1 = \varepsilon_y(-x\sin(\Delta\theta) + y\cos(\Delta\theta))$, so that X_1 and X_2 are in the directions of propagation of their respective groups. For simplicity, we will consider the case $A_1(X_1 = 0, Y_1 = 0) = A_2(X_2 = 0, Y_2 = 0) = a_0/2$, so that the linear amplitude at the point and time of focus $\eta^{(1)}(x = 0, y = 0, t = 0) = a_0$.

1) EULERIAN

At the sub-harmonic level, the second-order surface is again made up from a Eulerian set-down $\eta^{(2)}_{\mathrm{E,SD}} \equiv -(1/g)\partial\phi^{(2)}_{\mathrm{E},-}/\partial t$ and a cross-wave term $\eta^{(2)}_{\mathrm{E,CW}} \equiv \eta^{(2)}_{\mathrm{E,LF},-}$ (11). Both have been evaluated by McAllister et al. (2018). As for the case of the weakly spread group, the magnitude of the set-down depends inversely on depth $k_0 d$ and is generally small in deep water. The expression for the set-down is only marginally marginally less cumbersome than the multi-chromatic second-order theory reviewed in §2.b and we thus do not evaluate it here. The cross-wave term gives (McAllister et al. 2018):

$$\eta^{(2)}_{\mathrm{E,CW}} = \frac{1}{2}(1-\cos(\Delta\theta))k_0 A_1 A_2 \cos(\varphi_1 - \varphi_2), \tag{23}$$

where $\varphi_1 - \varphi_2 = x(1-\cos(\Delta\theta)) - y\sin(\Delta\theta) + \mu_1 - \mu_2$. Although the set-down is always slowly varying in both time and space, the crossing-wave contribution (23) responsible for a set-up is slowly varying in time, but rapidly varying in space. A partial standing wave pattern forms with lines of constant phase at an angle $\Delta\theta/2$ to the x-axis, namely in line with the bisection of the paths of travel of the two groups. Non-dimensionally, we thus have for the sub-harmonic part of the Eulerian second-order free surface elevation at the crossing point (i.e. $\tilde{\eta}^{(2)} \equiv \eta^{(2)}(x=0, y=0)/(k_0 a_0^2/2)$ with $A_1(X_1=0,Y_1=0) = A_2(X_2=0,Y_2=0) = a_0/2$),

$$\tilde{\eta}^{(2)}_{\mathrm{E},-} = \tilde{\eta}^{(2)}_{\mathrm{E,SD}} + \frac{1}{4}(1-\cos(\Delta\theta))\cos(\mu_1 - \mu_2). \tag{24}$$

At the super-harmonic level, terms arise from both the second-order potential $\phi^{(2)}_{+}$ and the linear forcing $\eta^{(2)}_{\mathrm{E,LF},+}$ (cf. (5)). For the latter, we obtain from substituting (21) and (22) into (11):

$$\begin{aligned}\eta^{(2)}_{\mathrm{E,LF},+} =& \frac{k_0 A_1(X_1,Y_1)^2}{2}\cos(2\varphi_1) + \frac{k_0 A_2(X_2,Y_2)^2}{2}\cos(2\varphi_2) \\ &- \frac{k_0 A_1(X_1,Y_1)A_2(X_2,Y_2)}{2}\cos(\Delta\theta)\cos(\varphi_1+\varphi_2).\end{aligned} \tag{25}$$

Substituting (21), (22) and (25) into (4) gives to leading order for $\phi_+^{(2)}$

$$\begin{aligned}\phi_{\mathrm{E},+}^{(2)} = &-\frac{2\left(1-\cos(\Delta\theta)\right)\omega_0 A_1(X_1,Y_1)A_2(X_2,Y_2)}{4-\sqrt{2+2\cos(\Delta\theta)}\tanh\left(k_z d\right)}\\ &\times\frac{\cosh\left(k_z(z+d)\right)}{\cosh\left(k_z d\right)}\sin(\varphi_1+\varphi_2),\end{aligned} \tag{26}$$

where $k_z \equiv \sqrt{2+2\cos(\Delta\theta)}k_0$. It is clear from (26) that the potential only has super-harmonics in the case of crossing ($\Delta\theta \neq 0$). Substituting (26) into (5) combined with (25) gives the total Eulerian super-harmonic second-order free surface elevation. In non-dimensional form, we thus obtain at the crossing point (i.e. $\tilde{\eta}^{(2)} \equiv \eta^{(2)}(x=0,y=0)/(k_0 a_0^2/2)$ with $A_1(X_1=0,Y_1=0) = A_2(X_2=0,Y_2=0) = a_0/2$),

$$\begin{aligned}\tilde{\eta}_{\mathrm{E},+}^{(2)} = &\frac{1}{4}\cos(2\varphi_1)+\frac{1}{4}\cos(2\varphi_2)\\ &+\left(\frac{1}{4}\left(3-\cos(\Delta\theta)\right)-\frac{2\left(1-\cos(\Delta\theta)\right)}{4-(k_z/k_0)\tanh\left(k_z d\right)}\right)\cos(\varphi_1+\varphi_2),\end{aligned} \tag{27}$$

where $k_z \equiv \sqrt{2+2\cos(\Delta\theta)}k_0$ as before. When two waves travel in the same direction ($\Delta\theta = 0$) and have the same phase ($\mu_0 \equiv \mu_1 = \mu_2$), we obtain $\tilde{\eta}_{\mathrm{E},+}^{(2)} = \cos(2\varphi_0)$, as for the case of a weakly spread group (cf. (15)). When two waves travel in the opposite direction ($\Delta\theta = 180^\circ$) and have the same phase ($\mu_0 \equiv \mu_1 = \mu_2$), we obtain $\tilde{\eta}_{\mathrm{E},+}^{(2)} = (1/2)\cos(2\varphi_0)$, which is equivalent to the super-harmonic terms derived for standing waves by Tadjbakhsh and Keller (1960) (their equation (46), see also Rayleigh (1915); Penny and Price (1952)).

2) LAGRANGIAN

Using the linear solutions for two crossing groups (21-22) to evaluate the Lagrangian second-order correction defined in (9) gives in non-dimensional form (i.e. $\tilde{\eta}^{(2)} \equiv \eta^{(2)}(x=0,y=0)/(k_0 a_0^2/2)$ with $A_1(X_1=0,Y_1=0) = A_2(X_2=0,Y_2=0) = a_0/2$),

$$\begin{aligned}\Delta\tilde{\eta}_{\mathrm{L}}^{(2)} = &\frac{1}{2}-\frac{1}{4}\cos(2\varphi_1)-\frac{1}{4}\cos(2\varphi_2)\\ &+\frac{1}{2}\cos(\Delta\theta)\left(\cos(\varphi_1-\varphi_2)-\cos(\varphi_1+\varphi_2)\right).\end{aligned} \tag{28}$$

When combined with the Eulerian free surface (27), the total Lagrangian second-order super-harmonic contribution is given by:

$$\eta^{(2)}_{\mathrm{L},+} = (1-\cos(\Delta\theta))\left(\frac{3}{4} - \frac{2}{4-\sqrt{2+2\cos(\Delta\theta)}}\right) \times \cos(\varphi_1+\varphi_2). \tag{29}$$

which is only non-zero when waves cross ($\Delta\theta \neq 0$), as the super-harmonics due to self interaction are not present in the Lagrangian signal.

If we consider only mean terms, we obtain the total Lagrangian second-order sub-harmonic contribution,

$$\eta^{(2)}_{\mathrm{L},-} = \tilde{\eta}^{(2)}_{\mathrm{E,SD}} + \frac{1}{2} + \frac{1}{4}(1+\cos(\Delta\theta))\cos(\mu_1-\mu_2), \tag{30}$$

which decays with increasing crossing angle.

3) Stokes drift velocity and Lagrangian frequency

To estimate the change in the Lagrangian frequency, we obtain the Stokes drift from (18) and evaluate the component travelling in the x-direction at the crossing point ($x=0$, $y=0$) and at $z=0$,

$$u_{\mathrm{S}} = \frac{1}{4}a_0^2 k_0 \omega_0 \left((1+\cos(\Delta\theta)) + 2\cos^4(\Delta\theta/2)\right), \tag{31}$$

where we have set $A_1(X_1=0,Y_1=0) = A_2(X_2=0,Y_2=0) = a_0/2$. For $\Delta\theta = 0$, we recover the Stokes drift of a weakly spread group (19) and for $\Delta\theta = 180^\circ$, the Stokes drift is zero. The corresponding Doppler-shifted Lagrangian frequency is,

$$\omega_{\mathrm{L},0} = \omega_0\left(1 - \frac{1}{4}a_0^2k_0^2\left((1+\cos(\Delta\theta)) + 2\cos^4(\Delta\theta/2)\right)\right). \tag{32}$$

e. A single strongly spread wave group (SSG)

When the degree of spreading becomes large, the model for a weakly spread group, in which directional spreading is captured by the modulation (in the y-direction) of a planar carrier wave (travelling in the x-direction), becomes invalid. To examine what is predicted for a strongly spread wave group (SSG), we consider the continuous generalization of (6-7), in which the directional and frequency (wavenumber magnitude) distributions are assumed independent, a standard assumption. In polar coordinates, $r = \sqrt{x^2+y^2}$ and $\theta_p = \text{atan}(y/x)$, we obtain for the linear free surface,

$$\eta^{(1)} = \int_{-\infty}^{\infty}\int_{-\pi}^{\pi} \Omega(\theta)\hat{\eta}(k)\cos(kr\cos(\theta-\theta_p)-\omega t+\mu)\mathrm{d}\theta\mathrm{d}k, \tag{33}$$

and the corresponding linear potential,

$$\phi^{(1)} = \int_{-\infty}^{\infty}\int_{-\pi}^{\pi} \frac{\omega}{k}\Omega(\theta)\hat{\eta}(k)e^{kz}\sin(kr\cos(\theta-\theta_p)-\omega t+\mu)\mathrm{d}\theta\mathrm{d}k, \tag{34}$$

where $k = |\mathbf{k}|$ and $\omega(k)$ and $\mu(k)$ in general. We will now consider the limit of a spectrum that is narrow-banded in frequency (wavenumber magnitude) but has arbitrary directional spreading, so that (33-34) become

$$\eta^{(1)} = a_0\int_{-\pi}^{\pi} \Omega(\theta)\cos(k_0 r\cos(\theta-\theta_p)-\omega_0 t+\mu_0)\mathrm{d}\theta, \tag{35}$$

$$\phi^{(1)} = \frac{a_0\omega_0}{k_0}\int_{-\pi}^{\pi} \Omega(\theta)e^{k_0 z}\sin(k_0 r\cos(\theta-\theta_p)-\omega_0 t+\mu_0)\mathrm{d}\theta, \tag{36}$$

where ω_0 and k_0 are the frequency and wavenumber of the carrier wave. We have not retained any of the group structure, so that (35-36) present crossing periodic wavetrains. To enable closed-form solutions where possible, we will make use of a wrapped normal spreading distribution centered around $\theta = \theta_0$ with characteristic spreading width σ_θ:

$$\Omega(\theta) = \frac{1}{\sqrt{2\pi}\sigma_\theta}\sum_{n=-\infty}^{\infty}\exp\left(-\frac{(\theta-\theta_0+2\pi n)^2}{2\sigma_\theta^2}\right). \tag{37}$$

1) EULERIAN

At the sub-harmonic level, the second-order surface is again made up from a Eulerian set-down $\eta^{(2)}_{\mathrm{E,SD}} \equiv -(1/g)\partial\phi^{(2)}_{\mathrm{E},-}/\partial t$ and a cross-wave term $\eta^{(2)}_{\mathrm{E,CW}} \equiv \eta^{(2)}_{\mathrm{E,LF},-}$ (11) (cf. (5)). As for the crossing wave groups, the Eulerian set-down term is driven by the return flow, and its magnitude will depend inversely on depth $k_0 d$ and thus be comparatively small for the deep-water conditions ($k_0 d \gg 1$) considered here. Because of this and since the set-down term can only be evaluated in the form of a triple integral that is only marginally less cumbersome than the multi-chromatic second-order theory reviewed in §2.b, we do not evaluate it here.

The linear forcing term $\eta^{(2)}_{\mathrm{E,LF}}$ is not directly affected by depth, and we can find an expression for a narrow-banded frequency distribution by substituting (35-36) into (11). Retaining both sub- and super-harmonic terms, we obtain at the crossing point $r = 0$ and after non-dimensionalization (i.e. $\tilde{\eta}^{(2)} \equiv \eta^{(2)}(r=0)/(k_0 a_0^2/2)$):

$$\begin{aligned}\tilde{\eta}^{(2)}_{\mathrm{E,LF}} = \frac{1+3\cos(2\varphi_0)}{2} \int_{-\pi}^{\pi}\int_{-\pi}^{\pi} \Omega(\theta_1)\Omega(\theta_2) d\theta_1 d\theta_2 \\ - \frac{1+\cos(2\varphi_0)}{2} \int_{-\pi}^{\pi}\int_{-\pi}^{\pi} \Omega(\theta_1)\Omega(\theta_2)\cos(\theta_1-\theta_2)\,\mathrm{d}\theta_1 \mathrm{d}\theta_2,\end{aligned} \tag{38}$$

where $\varphi_0 = \varphi_0(r=0) = -\omega_0 t + \mu_0$. For the wrapped normal distribution (37), the integrals in (38) can be evaluated explicit to give:

$$\tilde{\eta}^{(2)}_{\mathrm{E,LF}} = \frac{1}{2}\left(1 - e^{-\sigma_\theta^2}\right) + \frac{1}{2}\left(3 - e^{-\sigma_\theta^2}\right)\cos(2\varphi_0), \tag{39}$$

where we can confirm, in the limit $\sigma_\theta \to 0$, the sub-harmonic term vanishes and the super-harmonic term approaches its weakly spread counterpart (12).

Considering only sub-harmonic terms, for a strongly spread wave group we thus have,

$$\tilde{\eta}^{(2)}_{\mathrm{E},-} = \tilde{\eta}^{(2)}_{\mathrm{E,SD}} + \frac{1}{2}\left(1 - e^{-\sigma_\theta^2}\right). \tag{40}$$

From comparison with the weakly spread group ((15), for which $\tilde{\eta}^{(2)}_{\mathrm{E,SD}} = -1/(2k_0d(1+R))$), it is evident that non-weak directional spreading introduces a set-up of the Eulerian sub-harmonics free surface, as is predicted for crossing groups (see McAllister et al. (2018) and §2.d). This set-up vanishes in the limit $\sigma_\theta \to 0$, increases monotonically with the degree of spreading σ_θ and reaches a maximum for axisymmetric waves $\sigma_\theta \to \infty$.

Considering only super-harmonic terms, it is possible to solve Laplace subject to (4) and the bottom boundary condition to give:

$$\begin{aligned}\phi^{(2)}_{\mathrm{E},+} = -\omega_0 a_0^2 \int_{-\pi}^{\pi}\int_{-\pi}^{\pi} \frac{\cosh\left(k_z(z+d)\right)}{\cosh\left(k_z d\right)} \frac{2\left(1-\cos(\Delta\theta)\right)}{4-(k_z/k_0)\tanh\left(k_z d\right)} \\ \times \sin\left(k_0 r\cos(\theta_1-\theta_p) + k_0 r\cos(\theta_1-\theta_p) - 2\omega_0 t + 2\mu_0\right) \\ \times \Omega(\theta_1)\Omega(\theta_2)\mathrm{d}\theta_1\mathrm{d}\theta_2,\end{aligned} \tag{41}$$

where $\Delta\theta \equiv \theta_2 - \theta_1$ and $k_z \equiv \sqrt{2+2\cos(\Delta\theta)}k_0$. We note that super-harmonics only appear for non-zero spreading. We can then obtain for the super-harmonic free surface elevation at second order in non-dimensional form:

$$\tilde{\eta}^{(2)}_{\mathrm{E},+} = \left(\frac{3}{2} + F\left(k_0 d, \sigma_\theta\right) - \frac{1}{2}e^{-\sigma_\theta^2}\right)\cos(2\varphi_0), \tag{42}$$

where, for the wrapped normal distribution (37), the function $F\left(k_0 d, \sigma_\theta\right)$ is given by:

$$F = \frac{-2}{\sqrt{\pi}\sigma_\theta}\int_{-\infty}^{\infty} e^{-(\Delta\theta/\sigma_\theta)^2/4}\frac{1-\cos(\Delta\theta)}{4-(k_z/k_0)\tanh\left(k_z d\right)}\mathrm{d}\Delta\theta, \tag{43}$$

with $k_z \equiv \sqrt{2+2\cos(\Delta\theta)}k_0$ as before. We can recover the limit $\tilde{\eta}^{(2)}_{\mathrm{E},+} = \cos(2\varphi_0)$ for $\sigma_\theta \to 0$ ($F \to 0$) (cf. (15)). In the limit of an axisymmetric wave ($\sigma_\theta \to \infty$), we obtain a small in-phase contribution to the free surface by the super-harmonic of $\tilde{\eta}^{(2)}_{\mathrm{E},+} \approx 0.19\cos(2\varphi_0)$ in the limit $k_0 d \to \infty$ ($F \approx -1.31$, from numerical integration).

2) LAGRANGIAN

Using the linear solutions for a strongly spread group (35) and (36) to evaluate the Lagrangian second-order correction defined in (9) gives in non-dimensional form (i.e. $\tilde{\eta}^{(2)} \equiv \eta^{(2)}(r = 0)/(k_0 a_0^2/2)$),

$$\Delta\tilde{\eta}_{\mathrm{L}} = \int_{-\pi}^{\pi}\int_{-\pi}^{\pi} \Omega(\theta_2)\Omega(\theta_1)\cos(\theta_1-\theta_2)(1-\cos(2\varphi_0))d\theta_2 d\theta_2, \tag{44}$$

which can be evaluated explicitly for the wrapped normal distribution (37):

$$\Delta\tilde{\eta}_{\mathrm{L}}^{(2)} = e^{-\sigma_\theta^2}(1-\cos(2\varphi_0)). \tag{45}$$

The total Lagrangian free surface elevation for a strongly spread group is:

$$\begin{aligned}\tilde{\eta}_{\mathrm{L}}^{(2)} = \tilde{\eta}_{\mathrm{E,SD}}^{(2)} + \frac{1}{2}\left(1+e^{-\sigma_\theta^2}\right) \\ \left(-\frac{1}{2} + F\left(k_0 d, \sigma_\theta\right) + \frac{1}{2}e^{-\sigma_\theta^2}\right)\cos(2\varphi_0).\end{aligned} \tag{46}$$

3) STOKES DRIFT VELOCITY AND LAGRANGIAN FREQUENCY

To estimate the change in the Lagrangian frequency, we obtain the Stokes drift from (18) and evaluate the component travelling in the x-direction at the crossing point ($r = 0,\ \theta_p = 0$) and at $z = 0$ for the wrapped normal distribution (37):

$$u_{\mathrm{S}}(r=0, z=0) = \frac{a_0^2 k_0 \omega_0}{4}\left(3e^{-\sigma_\theta^2/2} + e^{-5\sigma_\theta^2/2}\right). \tag{47}$$

We thus obtain for the Lagrangian wave frequency:

$$\omega_{\mathrm{L},0} = \omega_0\left(1 - \frac{a_0^2 k_0^2}{4}\left(3e^{-\sigma_\theta^2/2} + e^{-5\sigma_\theta^2/2}\right)\right), \tag{48}$$

which becomes equal to the analogous result for the weakly spread group (20) in the limit $\sigma_\theta \to 0$. As $\sigma_\theta \to \infty$, the Stokes drift disappears, and the Lagrangian period becomes equal to the Eulerian period ($\omega_{\mathrm{L},0} \to \omega_0$).

f. Comparison with multi-component second-order theory

Table 1 summarizes the results for the three cases considered above. We will now compare our approximate second-order expressions to exact multi-component second-order theory from HJ16 for narrow-banded spectra (§2.f.1) and for realistic broad-banded spectra (§2.f.2).

1) NARROW-BANDED SPECTRA

Figures 1.a-c compare the normalised amplitude ($\tilde{a}^{(2)} = a^{(2)}/(k_0 a_0^2/2)$ with $a^{(2)}$ denoting the amplitude of $\eta^{(2)}$) of sub- and super-harmonics predicted using exact second-order theory (solid lines) to our approximate expressions (dotted lines) for a single wave group as a function of the degree of directional spreading σ_θ. Red lines show the magnitude of the Eulerian components $\tilde{a}_{\mathrm{E}}^{(2)}$, grey the Lagrangian correction $\tilde{a}_{\Delta\mathrm{L}}^{(2)}$, and blue the magnitude of the Lagrangian components $\tilde{a}_{\mathrm{L}}^{(2)}$. We choose the water depth $k_0 d = 3.94$ to correspond to our experiments, and the discrepancy between our approximate solutions (dotted lines) and exact second-order theory (solid lines) in figure 1 comes from excluding the set-down in our approximate solutions. Figures 1.d-f are analogous to figures 1.a-c, but illustrate the second-order amplitude for two crossing wave groups as a function of the crossing angle $\Delta\theta$. As expected, our approximate expressions compare well with exact theory for wave groups with a narrow underlying spectrum ($\Delta k/k_0 = 0.05$) given explicitly by:

$$\hat{\eta}(k) = \frac{a_0}{\sqrt{2\pi}\Delta k} \exp\left(-\frac{1}{2}\left(\frac{k-k_0}{\Delta k}\right)\right). \tag{49}$$

Examining trends in figure 1, in the limit of no spreading or crossing ($\sigma_\theta \to 0$, $\Delta\theta \to 0$), the amplitude of the Eulerian second-order sub-harmonics (figure 1.a,e) is small and equal to the set-down $\tilde{\eta}_{\mathrm{E,SD}}^{(2)}$, which vanishes for truly deep water ($k_0 d \to \infty$). The Lagrangian correction is at its maximum. As the degree of spreading or the crossing angle is increased, a positive Eulerian set-up forms and the Lagrangian correction tends to zero. Therefore, in the limit ($\sigma_\theta \to \infty$, $\Delta\theta \to$

180), Eulerian and Lagrangian second-order components become equal. The same is true for super-harmonic components (figure 1.c,f), which also tend towards each other in the limit of large spreading or head-on crossing ($\Delta\theta \to 180$). However, without spreading or crossing, Eulerian super-harmonic components are at their largest and are completely cancelled out by the Lagrangian correction, which is negative. When combined, the sub- and super-harmonic components of the Lagrangian correction completely cancel out (figure 1.c,f). Thus, for narrow-banded wave groups on deep water, the total second-order contribution to crest height for Eulerian and Lagrangian measurements is equal.

2) REALISTIC BROAD-BANDED SPECTRA

Our approximate expressions for second-order contribution to crest-height are derived using the assumption that the spectra that underlie our wave groups are narrow-banded in frequency. In reality, ocean waves typically follow relatively broad-banded frequency distributions with a slowly decaying high-frequency tail. To estimate how well our approximate expressions perform for realistic broad-banded spectra, we compare these with predictions made using exact second-order theory for a focused wave groups based on a JONSWAP spectrum (Hasselmann et al. 1980):

$$\hat{\eta}(\omega) = \beta\omega^n \exp\left[\frac{n}{4}\left(\frac{\omega_p}{\omega}\right)^4\right]\gamma^{\exp\left[\frac{-(\omega-\omega_p)^2}{2\sigma^2\omega_p^2}\right]}, \tag{50}$$

where γ is the peak enhancement factor, ω_p is the peak frequency, n is the slope of the high frequency tail, $\sigma(\omega < \omega_p) = 0.07$ and $\sigma(\omega > \omega_p) = 0.09$, and β is a scale parameter which is adjusted to give the desired amplitude. We emphasize again we let the amplitude spectrum to be proportional to the energy spectrum in (50), as this provides a good (and commonly used) approximation to the shape of extreme waves in the ocean (Lindgren 1970; Boccotti 1983; Phillips et al. 1993).

In Fig. 2, we compare predictions made using our approximate expressions (29) and (30) (dotted lines) to predictions made using exact second-order theory for wave groups based on Gaussian ($\Delta k = 0.6$ m^{-1}, dashed lines) and JONSWAP spectra ($\gamma = 3.3$, $n = -5$, solid lines). The relatively broad-banded Gaussian spectrum ($\Delta k/k_0 = 0.30$) is what we use in our experiments. For the relatively broad-banded Gaussian spectrum, our approximate expressions for the super-harmonic components follow predictions made using exact second-order well. However, when considering sub-harmonic components, a clear offset is observed. This offset occurs because we do not include in our approximate expressions the Eulerian set down term $\tilde{\eta}_{\mathrm{E,SD}}$ (without crossing and spreading, we can readily estimate $\tilde{\eta}_{\mathrm{E,SD}} = -0.13$ for $k_0 d = 3.9$ from (15)). For the JONSWAP spectrum in Fig. 2, our approximate expressions perform very well with only a small error from not including the set-down. When the same calculations are performed for an increased water depth ($k_0 d = 7.9$), this offset is reduced (dot-dashed lines). Our approximate expressions become more accurate for realistic spectra when the water depth becomes truly deep and the set-down can be entirely ignored, as expected. Examining directionally spread groups gives qualitatively and quantitatively similar results.

3. Experimental method

In this section, we first introduce our experimental set-up (§3.a). We then detail the input parameters we use for our experiments and the process used to estimate the spectral and directional parameters achieved in the tank (§3.b). Finally, in §3.d we discuss sources of measurement error and the repeatability of our experiments.

a. Experimental set-up

The experiments presented herein were carried out in the FloWave Ocean Energy Research Facility at the University of Edinburgh. This is a circular wave basin, which is 2 m deep and surrounded by 168 actively-absorbing force-feedback wavemakers, which allows for the creation of waves that travel in any direction. With the exception of the Lagrangian wave measurements, the experimental set-up and procedure follows exactly that of McAllister et al. (2018). Eulerian measurements of free surface elevation were made using resistive wave gauges, which were calibrated at the start of each day of testing. Any Eulerian measurements presented herein are at the intended point of focus in the centre of the tank ($x = 0$, $y = 0$).

Although waves are in principle absorbed by the wavemakers, this process is not perfect, and reflections may still occur. To avoid reflections, we set the run time of our experiments to 32 s, and allowed for 10 min of settling time between each experiment to ensure the dissipation of any background motion in the tank.

To measure free surface elevation, wave-following buoys first measure acceleration, which is then integrated twice to give displacement. These displacements are projected onto the coordinate system of heave, North, and East displacements. In our experiments, we assume that there is no error in this process (see Van Essen et al. (2018); Raghukumar et al. (2019) for a discussion of this assumption), and consider the position of our model buoy to be what a wave buoy in the ocean would measure.

We measure the position of our model buoy using a Qualisys motion tracking system, consisting of four calibrated infra-red cameras located above the tank, which simultaneously track the position of the buoy. To aid its detection, the spherical model buoy was covered in a coating

that reflects the specific band of infra-red light emitted and recorded by the cameras. The buoy's position in each set of images is then triangulated to measure its global position within the tank.

1) Model Lagrangian buoy

Wave-following measurement buoys are in general spherical to avoid sensitivity to yaw, pitch, and roll motion. These properties are measured by other types of, typically larger, weather buoys, which often measure a range of metocean conditions, such as wind speed in addition to wave height. As the latter of these two types of buoys behaviour is far from Lagrangian, they will not be considered in this study.

Wave-following buoys typically have diameters in the range of $0.5-1$ m and operate on water depths from tens to thousands of metres, in waves of 1 to 30 m in height and 1 to 20 s in period. This wide range of operating conditions presents a challenge for scaling. If a floating body's characteristic length (diameter) is of the same order as the length of the waves incident on it, its motion will cause diffraction and radiation. To correctly scale these effects, similar ratios of buoy diameter to incident wavelength, D/λ, must be maintained between our model and a buoy operating in the ocean. The density of our buoy was chosen to be approximately half that of the water, to match that of a real measurement buoy.

The diameter of a buoy will also affect the forces that dominate its motion. If the fluid velocity relative to a buoy's size is large, drag forces will dominate and, conversely, if velocity is low, inertial forces will dominate. The Keulegan-Carpenter number, which can be approximated for a stationary body in periodic linear waves as $\mathrm{K_C} = 2\pi a_0/D$, is often used to characterise the relative importance of these two forces. A wave-following buoy will not be stationary, and if purely Lagrangian its velocity relative to the fluid will tend to zero. This makes it difficult to correctly evaluate the $\mathrm{K_C}$ number a priori. In light of this, we do not directly evaluate the $\mathrm{K_C}$. However, it is

worthwhile checking that the ratio of our buoy's diameter to wave amplitude D/a_0 is of a similar order to that of a real buoy. Finally, the water depth $k_0 d$ on which a buoy operates will affect the kinematics of the incident waves.

Our study is motivated by extreme ocean waves. Our experiments have $k_0 d \approx 4$, representative of deep-water conditions (typically, $k_0 d \gtrsim 3$). Increasing water depth further will not affect the resulting linear kinematics and will, at second-order, only affect the magnitude of the set-down, which is already small (cf. figures 1 and 2), and very slightly the Eulerian super-harmonic for large crossing angles and degrees of spreading. Mooring designs will change with increasing water depth, but we do not consider the effects of mooring herein. Extreme ocean waves will typically have long periods in the range 10-20 s; for a 1.0 m buoy on deep water, this gives the range $D/\lambda = 1.6 \times 10^{-3}$-$6.4 \times 10^{-2}$. The diameter of our model buoy is 0.07 m, and the peak period of the waves we test is 1.43 s, which gives $D/\lambda = 3.6 \times 10^{-2}$. Therefore, at both scales, $D/\lambda \ll 1$, meaning diffraction, radiation, and hydrodynamic resonance will not play a significant role. Extreme wave crest heights or amplitudes may range between $5-15$ m; for a 1.0 m buoy this gives ratios of $a_0/D =$ 5-15. The wave amplitudes we tests result in ratios of around $a_0/D =$ 2.14-2.86. These values are somewhat lower than the most extreme waves. Testing with a smaller buoy was not possible, as reliably tracking the motion of very small buoy becomes difficult, and the auxiliary mooring forces discussed below become dominant and start to affect buoy motion.

Ideally, to perform a comparison of predicted Lagrangian motion to the actual Lagrangian motion of our buoy, the buoy would have no mooring. However, an auxiliary mooring was necessary to achieve readily repeatable experiments. Additional experiments were carried out with no auxiliary mooring, and it was found that the mooring had no observable effect on the measured freesurface elevation including bound wave components. We emphasise that the effect of a mooring on buoy motion in a realistic configuration is not the objective of the present study.

b. Matrix of experiments and input parameters

To recreate conditions representative of extreme events that occur in the oceans, we examine focused wave groups (Lindgren 1970; Boccotti 1983; Phillips et al. 1993). We carry out two categories of experiments (see table 2): experiments with (weakly and strongly) spread wave groups (§3.b.1) and experiments with crossing wave groups (§3.b.2). In the first category, we vary the degree of directional spreading for a single group and, in the second category, the angle at which two wave groups cross.

For all experiments, we produced focused wave groups based on a input Gaussian amplitude distribution in wavenumber $k = |\mathbf{k}|$,

$$\hat{\eta}(k) = \frac{a_0}{\sqrt{2\pi}\Delta k} \exp\left(-\frac{1}{2}\left(\frac{k-k_0}{\Delta k}\right)\right), \tag{51}$$

with peak wavenumber $k_0 = 1.97$ m^{-1} (based on a frequency of 0.7 Hz) and standard deviation $\Delta k = 0.6$ m^{-1}. The value a_0 is adjusted to give the desired wave steepness. We carry out experiments at two steepness, $a_0 k_0 = 0.3$ and 0.4; these high steepnessess were chosen to replicate extreme ocean waves and generate large and hence readily measurable second-order bound components without causing wave breaking. We define our inputs using this form to allow for consistency with the second-order theory presented in §2. The input parameters we use are a chosen to fit within the optimum generation range of the wavemakers, whilst achieving a relatively spatially compact wave group to minimise the influence of reflections and error waves associated with linear wave paddle motion. We define directional spreading using a Gaussian amplitude distribution in angle θ,

$$\Omega(\theta) = \frac{\Omega_0}{\sqrt{2\pi}\sigma_\theta} \sum_{n=-N}^{N} \exp\left(-\frac{(\theta-\theta_0+2\pi n)^2}{2\sigma_\theta^2}\right), \tag{52}$$

where we set the normalising coefficient Ω_0 so that the sum of $\Omega(\theta)$ over the finite number of components N is unity. For crossing wave groups, two amplitude distributions with different

values of θ_0 are superimposed. It should be noted that our value of σ_θ applies to an amplitude distribution and not the commonly used energy spectrum for which the degree of spreading will be equal to $\sigma_\theta/\sqrt{2}$.

1) Experiments with spread wave groups

We first examine single directionally spread wave groups (see table 2). We vary spreading from unidirectional ($\sigma_\theta = 0^\circ$) to axisymmetric ($\sigma_\theta \to \infty$) at an input steepness of $a_0 k_0 = 0.3$. We repeat experiments for an unmoored buoy at spreading widths of $20, 40$, and ∞°. We also carry out additional experiments for our moored buoy at increased steepness $a_0 k_0 = 0.4$.

2) Experiments with crossing wave groups

In addition to single wave groups, we examine the Lagrangian measurement of extreme crossing wave groups (see table 2). For these experiments, we set the directional spreading of each group $\sigma_\theta = 20^\circ$ and vary the angle at which the two wave groups cross $\Delta\theta$ between 0 and 180° at 45° intervals. The steepness of the two combined wave groups was set as $a_0 k_0 = 0.3$.

c. Estimation of spectral and directional parameters

To verify the test conditions achieved in the tank, we estimate the spectral parameters of our measured free surface elevation. This is carried out for both Eulerian and Lagrangian measurements (see table 3). To estimate the linear amplitude $a_0^\star$ of each wave group, we take the zeroth moment of the measured linear spectrum, as this provides an estimate of amplitude that is less sensitive to focusing than using crest amplitude. For both the Eulerian and the Lagrangian measurements, we estimate peak frequency $\omega_0^\star$ and quantify the spectral bandwidth $\Delta\omega^\star$ as the variance of the measured spectra.

To estimate the degree of directional spreading achieved for each experiment $\sigma_\theta^\star$, we use Eulerian measurements made with an array of 14 wave gauges. Owing to the non-ergodic nature of our experiments, we cannot apply conventional methods of spreading estimation. Instead, we use a least-squares approach combined with linear wave theory to determine the degree of spreading $\sigma_\theta^\star$ (see McAllister et al. (2018)). Input and estimated parameters are reported in table 3.

d. Measurement error and repeatability

To quantify the sources of error affecting our comparison between experiments and theory, we examine the role of the various sources of error and uncertainty involved in our experiments. For the Eulerian measurements, McAllister et al. (2018) found that the leading source of error was most likely associated with wave gauge calibration ($\pm\Delta\eta_\mathrm{E} \approx 0.4$ mm), with residual tank motion and experiment repeatability resulting in errors of approximately ± 0.025 and ± 0.023 mm, respectively (two standard deviations). For the Eulerian measurements, McAllister et al. (2018) noted that tests carried out at larger amplitudes reduce the variation between repeat experiments. We carry out the majority of our experiments at the larger of the two amplitudes tested in McAllister et al. (2018).

Our Lagrangian measurements will be subject to similar sources of error. To understand these sources of error, we assess the repeatability of these measurements (error measure I) and compute the accuracy of the Qualisys motion tracking system (error measures II and III). The repeatability of our experiments was extremely high with twice the standard deviation of repeat experiments ranging from ± 0.08 to ± 1.00 mm. The error calculated when calibrating the Qualisys system error was slightly larger at approximately ± 0.5 mm, when measuring a distance of 300 mm, which is approximately the height of our waves. The leading source of error was associated with locating the buoy's position during experiments, where time-varying residual values ranged from around

± 0.5 to ± 1.5 mm. At every time stamp when the Qualisys system measures the position of the centroid of our model buoy, a residual value is returned. This value represents the diameter of a sphere, inside which all the centroids identified by each camera pair lie. We use these residual values measured during each experiment to calculate error bounds for the results we present herein.

4. Results

In this section, we present the results of our experiments and compare Eulerian and Lagrangian measurements of directionally spread and crossing wave groups. In §4.a, we examine differences in the measured linear free surface elevation. In §4.b, we then examine the second-order sub- and super-harmonics and their contribution to measured crest height; we also compare our results to predictions based on the theory we present in §2. Throughout, because of the near-perfect agreement, we will refer to measurements obtained from the model buoy as Lagrangian measurements.

a. Linear free surface elevation

We begin by comparing the linear free surface elevation measured by our Lagrangian buoy and Eulerian wave gauges (see McAllister et al. (2018) for details of our linearisation procedure). Figures 3.a, b show the linear free surface elevation measured by our Lagrangian buoy $\eta_{\mathrm{L}}^{(1)}$ (red dashed lines) to the corresponding Eulerian measurements $\eta_{\mathrm{E}}^{(1)}$ (black solid lines) for single directionally spread wave groups as the degree of spreading is increased from narrowly spread to near-axisymmetric. This figure shows the steepest wave groups we created, for which the input steepness was $a_0 k_0 = 0.4$. Panels c and d illustrate changes to the linear spectra $\hat{\eta}^{(1)}$; these changes are also quantified in Tab. 3. In Fig. 3, for narrow directional spreading σ_θ, the period of the Lagrangian measurements is increased; this is visible when considering the measured free surface elevation and the resulting amplitude spectrum.

Performing a direct comparison between values of Lagrangian frequency predicted by our approximate expressions to those measured during our experiments is challenging. The relativity broad-banded wave groups we create have an envelope that varies quickly, and hence so does the Lagrangian frequency, making it difficult to measure reliably. Instead, we include vertical dashed and dotted lines in Fig. 3.c and 3.d that show the measured peak frequency and corresponding approximate Lagrangian peak frequency obtained from (48). The comparison is intended to be qualitative. In narrowly-spread conditions (Fig. 3.c), our expression predicts a down-shift of the Lagrangian frequency, which compares well to the down-shift we observe in our experiments. On the contrary, in the limit of $\sigma_\theta \to \infty$ (Fig. 3.d) no Doppler shift is observed, which is also in line with our predictions. In general, as spreading is increased, either for a single group or two crossing waves, the difference between the Lagrangian and Eulerian period tends to zero.

Figure 4.a compares the amplitude of the waves measured by our model buoy (a_L) to their Eulerian equivalent (a_E) measured at the position of intended focus ($x = 0$, $y = 0$) across the full range of conditions we test (see Tab. 2). The red markers show the full crest amplitude amplitude measured by each device, and the black markers show the linearised crest amplitude. In general, for the smaller waves, both are approximately equal. However, for the larger amplitude waves, some of the Lagrangian measurements are greater than their Eulerian counterparts.

In Fig. 4.b, we compare the ratio of the linearised Lagrangian and Eulerian amplitudes $a_\mathrm{L}^{(1)}/a_\mathrm{E}^{(1)}$ as a function of the degree of directional spreading σ_θ (circles and triangles) and crossing angle $\Delta\theta$ (crosses). It should be noted values of $a^{(1)}$ we present are measured crest amplitudes, unlike values of $a_0^\star$, which are based on the zeroth spectral moment. A small increase in measured Lagrangian amplitude (compared to Eulerian) is only observed for unidirectional and very narrowly spread wave groups. We measured waves of equivalent amplitudes with large degrees of spreading and found no difference between Eulerian and Lagrangian measurements in that case (shown by the

triangles in upper portion of Fig. 4.a which lie on the line $a_{\mathrm{L}} = a_{\mathrm{E}}$. Therefore, we hypothesize this difference in linear amplitude is a phenomenon associated with the horizontal transport of the buoy beyond what is predicted by any second-order theory. The wave groups we create are broad-banded in frequency, meaning that they disperse and change shape significantly and rapidly as they propagate across the wave tank. When our wave groups are unidirectional or narrowly spread, the resulting horizontal transport of the buoy is at its largest. It is also the case that the most steep and narrowly spread wave groups we create focus slightly downstream of our central wave gauge. Hence, as Stokes drift causes the buoy to be transported downstream, it measures a slightly larger wave group than the Eulerian gauge, which is fixed at $x = 0$, $y = 0$.

b. Second-order free surface elevation

Figures 5 and 6 present the second-order sub- (top row) and super-harmonic (bottom row) bound waves from our experiments. In each panel, the black solid line shows the measured Eulerian free surface elevation at the intended point of focus ($x = 0$, $y = 0$), and the black dashed line shows the corresponding Lagrangian free surface elevation for the same incident wave group. The red dashed and blue dotted lines show predictions made using exact Eulerian and Lagrangian multi-component second-order theory, respectively. Both sets of predictions are based on the measured Eulerian linear free surface elevation $\eta_{\mathrm{E}}^{(1)}$.

1) DIRECTIONALLY SPREAD WAVE GROUPS

In figure 5, we consider directionally spread wave groups and we vary the degree of directional spreading. Moving from left to right, the input value of σ_θ is increased from 0 to 50° in 10° increments; the actual degree of spreading measured in the tank $\sigma_\theta^\star$ is displayed above each panel. The input amplitude a_0 of these wave groups was set to 0.15 m giving a steepness of $a_0 k_0 = 0.3$.

For both sub- and super-harmonic bound waves, the Eulerian measurements agree remarkably well for all degrees of spreading shown. As σ_θ initially increases, the amplitudes of both sub- and super-harmonic bound wave components decrease. However, as spreading is further increased, the Eulerian sub-harmonic components become large and positive, corresponding to the set-up studied in McAllister et al. (2018) (see also figure 7.b). Excluding the unidirectional case in figure 5.a, the measured Lagrangian bound wave components also match theoretical predictions very well. This discrepancy is a result of the increased linear amplitude measured by the buoy discussed above, as calculations are based on the linear Eulerian measurement. For all degrees of spreading, we observe a positive set-up when considering the Lagrangian sub-harmonic bound wave components, which decreases in amplitude as the degree of spreading is increased. The amplitude of the measured Lagrangian super-harmonic bound wave components is negligibly small for these experiments, as predicted for a perfectly Lagrangian observer for up to moderate degrees of directional spreading.

2) Crossing wave groups

In figure 6, we consider two crossing wave groups, each with input directional spread $\sigma_\theta = 20^\circ$ and a combined input steepness of $a_0 k_0 = 0.3$. We vary the angle at which the two wave groups cross. Moving left to right, the crossing angle is increased from 0 to 180° in increments of 45°. For these experiments, theoretical predictions match our experimental observations very well. At low crossing angles, the Lagrangian second-order bound wave components are similar to those observed in figure 5. When the waves cross at large angles, the Lagrangian bound wave components tend to their Eulerian equivalents; this also occurs for a single directional spread wave group when $\sigma_\theta \to \infty$ (cf. figure 7.b-d).

When waves cross at large angles or are highly directionally spread, the horizontal velocity they induce cancels out at the point of focus. Therefore, there is no horizontal motion, and the Lagrangian surface elevation recorded by a buoy is equivalent to the Eulerian surface elevation. At moderate crossing angles and degrees of spreading, Lagrangian measurements lie between two extremes, where on the one hand we essentially have standing waves with horizontal motion of the buoy tending to zero ($\eta_E = \eta_L$), and on the other hand we have the unidirectional limit where horizontal motion is the largest ($\eta_E \neq \eta_L$).

3) Contribution to crest amplitude

In figures 7 and 8, we examine the behaviour of the Eulerian and Lagrangian second-order bound components as functions of σ_θ and $\Delta\theta$ in more detail. In these figures, we present the magnitude of the second-order bound components normalised by the measured wavenumber $k_0^\star$ and amplitude $a_0^\star$ (see table 3). By combining sub- and super-harmonics, we also consider the total second-order contribution to crest amplitude. The continuous lines in these figures represent theoretical predictions of the magnitude of second-order bound components for perfectly focused Gaussian wave groups with the same parameters as our experiments. When normalised in this way, it becomes clear that the combined Lagrangian bound wave components do not decrease in magnitude monotonically with increasing σ_θ or $\Delta\theta$ (cf. figures 7.d and 8.d). Furthermore, when combined, the total second-order bound wave contribution of Eulerian and Lagrangian measurements do not differ significantly. Figures 7.a and 8.a illustrate that, under the conditions we test, the second-order motion of our buoy is the same as that of a perfectly Lagrangian observer.

4) TOTAL FREE SURFACE ELEVATION

Finally, figure 9 compares the total measured Eulerian η_E (black lines) and Lagrangian η_L (red dashed lines) free surface elevation for the steepest input waves we created ($a_0 k_0 = 0.4$). For steep near-breaking moderately spread wave groups (figure 9.a,b), we see differences between Eulerian and Lagrangian measurements, namely an apparent broadening of the wave crest. As spreading is further increased (figure 9.c), we do not observe differences in the measured time series. The observed difference in local wave steepness for moderately spread wave groups occurs as a result of two effects. First, changes to the Lagrangian linear waves makes their period longer than their Eulerian equivalents (cf. figure 3). Second, super-harmonic components make the measured Eulerian crests narrower and troughs broader. Therefore, although the total second-order contributions to crest amplitude do not differ significantly, for moderate degrees of spreading, the time series of Lagrangian and Eulerian measurements are different.

5. Conclusion

Wave measurement buoys are widely used to provide in-situ wave measurements. These measurements are used to calibrate ocean models, inform engineering design, and study ocean wave phenomena. Particularly when studying extreme waves, measurements generated by wave buoys are perceived to be less accurate than Eulerian measurements (Dysthe and Müller 2008). It should be noted that in the field, Eulerian wave measurements also fall prey to issues such sea spray and beam scattering that affect their accuracy (Forristall et al. 2004). In the field, as both sensor types are imperfect and are rarely located together, it is very difficult to directly assess their accuracy and identify particular sources error.

In lieu of direct comparison, various explanations are commonly given to explain why buoy measurements may underreport extreme wave crests. It is well understood that as waves become

steep, and their behaviour nonlinear, Eulerian and Lagrangian free surface measurements become fundamentally different (Longuet-Higgins 1986; Srokosz and Longuet-Higgins 1986; Herbers and Janssen 2016; Grue and Kolaas 2019). Therefore, it is often suggested that differences between Lagrangian and Eulerian measurements may cause the underestimation of extreme waves crest.

In this paper, we have derived a series of approximate second-order expressions that may be used to predict Eulerian and Lagrangian free surface elevation and Stokes drift velocity for extreme waves, which we compare to exact multi-component second-order theory of Herbers and Janssen (2016) (HJ16). The leading-order nonlinear effect of Lagrangian motion is a cancellation of second-order bound super-harmonics and a corresponding increase in amplitude of second-order sub-harmonic components. Although this constitutes a change in the frequency content of the second-order contributions to crest height measured by the two types of device, our theoretical predictions show that in deep water this does not result in a significant change to wave crest amplitude. This phenomenon essentially constitutes a shift of second-order bound energy from high (super-harmonics) to low (sub-harmonics) frequencies, as identified by HJ16. For devices that measure acceleration, where integration is required to convert to displacement, and data is implicitly high-pass filtered, this shifting of energy content may cause the underestimation of crest height (Marthinsen and Winterstein 1992; Prevosto et al. 2000; Forristall 2000). If a wave-following buoy behaves in a purely Lagrangian manner, there should be no significant differences in measured wave crests, assuming no error in the measurement acquisition process (see Van Essen et al. (2018)).

This raises an additional question whether wave-following buoys do in fact behave in a purely Lagrangian manner. Wave measurement buoys float on the surface, and have densities of approximately half that of sea water and hence may be subject to inertial (Santamaria et al. 2013; Pizzo et al. 2019) and slope sliding effects (Meylan et al. 2015) identified by these authors in different

physical contexts. Therefore, wave-following measurement buoys may not behave in a purely Lagrangian manner and, as is commonly perceived, they may avoid extreme wave crests (Krogstad and Barstow 2000).

We have carried out a series of laboratory experiments to assess whether the motion of a scaled wave-following buoy in extreme ocean waves is purely Lagrangian and have carried out a direct comparison between Eulerian and buoy measurements of steep directionally spread wave groups at laboratory scale. We have done so in a range of directionally spread conditions, including crossing. The second-order motion of our model buoy compares extremely well with predictions made using existing exact Lagrangian second-order theory (HJ16) and our novel approximate expressions. It is only in the most extreme cases we test, where the waves are unidirectional, that we note observable differences. In such cases, we see an apparent modification to the linear waves measured by the buoy, which we believe is a result of the fact that the buoy's displacement becomes large enough for our wave group to have dispersed and changed shape during its measurement. Otherwise, we find that buoy motion at the scale we test is well predicted by approximate and exact Lagrangian second-order theory. In the range of conditions we test, excluding near unidirectional conditions as discussed above, any deviation from Lagrangian motion of measurement buoys in the field is most likely a result of mooring forces or an artefact of internal signal processing. Future work will address the application of the findings in this paper to random sea states and real buoy data.

Acknowledgments. This project was funded by the EPSRC and Wave Energy Scotland (grant no. 24840078 and 24841554). TSvdB was supported by a Royal Academy of Engineering Research Fellowship. The authors would like to thank Mr E. Nixon, Dr. R. Gabl, and Dr T. Davey at the FloWave Ocean Energy Research Facility for their assistance in planning and carrying out the experiments.

References

Allender, J., T. Audunson, S. F. Barstow, S. Bjerken, H. E. Krogstad, P. Steinbakke, L. Vartdal, and C. G. L. E. Borgman, 1989: The WADIC project: A comprehensive field evaluation of directional wave instrumentation. *Ocean Eng.*, **16**, 505–536.

Ashton, I. G. C., and L. Johanning, 2015: On errors in low frequency wave measurements from wave buoys. *Ocean Eng.*, **95**, 11–22.

Benetazzo, A., and Coauthors, 2017: On the shape and likelihood of oceanic rogue waves. *Scientific reports*, **7**, 8276.

Bidlot, J., D. J. Holmes, P. A. Wittmann, R. Lalbeharry, and H. S. Chen, 2002: Intercomparison of the performance of operational ocean wave forecasting systems with buoy data. *Weather Forecast.*, **17**, 287–310.

Boccotti, P., 1983: Some new results on statistical properties of wind waves. *App. Ocean Res.*, **5**, 134–140.

Christou, M., P. Tromans, L. Vanderschuren, and K. Ewans, 2009: Second-order crest statistics of realistic sea states. *Proc. of the 11th Int. Workshop on Wave Hindcasting and Forecasting, Halifax, Canada*, 18–23.

Collins III, C. O., B. Lund, T. Waseda, and H. C. Graber, 2014: On recording sea surface elevation with accelerometer buoys: lessons from ITOP (2010). *Ocean Dynam.*, **64**, 895–904.

Dalzell, J. F., 1999: A note on finite depth second-order wave–wave interactions. *App. Ocean Res.*, **21**, 105–111.

Dysthe, K. B., and H. E. K. P. Müller, 2008: Oceanic rogue waves. *Annu. Rev. Fluid Mech.*, **40**, 287–310.

804 Fedele, F., and F. Arena, 2010: Long-term statistics and extreme waves of sea storms. *J. Phys.*
805 *Oceanog*, **40**, 1106–1117.

806 Forristall, G. Z., 2000: Wave crest distributions: Observations and second-order theory. *J. Phys.*
807 *Oceanogr.*, **30**, 1931–1943.

808 Forristall, G. Z., S. F. Barstow, H. E. Krogstad, M. Prevosto, P. H. Taylor, and P. S. Tromans,
809 2004: Wave crest sensor intercomparison study: an overview of WACSIS. *J. Offshore Mech.*
810 *Arct.*, **126**, 26–34.

811 Gemmrich, J., and J. Thomson, 2017: Observations of the shape and group dynamics of rogue
812 waves. *Geophysical Research Letters*, **44**, 1823–1830.

813 Grue, J., and J. Kolaas, 2019: On the Lagrangian period in steep periodic waves. *Water Waves*,
814 1–16.

815 Hasselmann, D. E., M. Dunckel, and J. A. Ewing, 1980: Directional wave spectra observed during
816 JONSWAP 1973. *J. Phys Oceanogr.*, **10**, 1264–1280.

817 Hasselmann, K., 1962: On the non-linear energy transfer in a gravity-wave spectrum part 1. Gen-
818 eral theory. *J. Fluid Mech.*, **12**, 481–500.

819 Herbers, T. H. C., S. Elgar, and R. T. Guza, 1994: Infragravity-frequency (0.005-0.05 Hz) motions
820 on the shelf. Part I: Forced waves. *J. Phys. Oceanogr.*, **24**, 917–927.

821 Herbers, T. H. C., and T. T. Janssen, 2016: Lagrangian surface wave motion and Stokes drift
822 fluctuations. *J. Phys. Oceanogr.*, **46**, 1009–1021.

823 Herbers, T. H. C., P. F. Jessen, T. T. Janssen, D. B. Colbert, and J. H. MacMahan, 2012: Observing
824 ocean surface waves with GPS-tracked buoys. *J. Atmospheric and Ocean. Technol.*, **29**, 944–
825 959.

826 Holthuijsen, L. H., and T. H. C. Herbers, 1986: Statistics of breaking waves observed as whitecaps
827 in the open sea. *J. Phys. Oceanogr.*, **16**, 290–297.

828 Janssen, P. A. E. M., B. Hansen, and J. Bidlot, 1997: Verification of the ECMWF wave forecasting
829 system against buoy and altimeter data. *Weather Forecast.*, **12**, 763–784.

830 Krogstad, H. E., and S. F. Barstow, 2000: A unified approach to extreme value analysis of ocean
831 waves. *The Tenth International Offshore and Polar Engineering Conference*.

832 Lenee-Bluhm, P., R. Paasch, and H. T. Özkan-Haller, 2011: Characterizing the wave energy re-
833 source of the US Pacific Northwest. *Renew Energ.*, **36**, 2106–2119.

834 Lindgren, G., 1970: Some properties of a normal process near a local maximum. *The Annals of*
835 *Mathematical Statistics*, **41**, 1870–1883.

836 Liu, Q., T. Lewis, Y. Zhang, and W. Sheng, 2015: Performance assessment of wave measurements
837 of wave buoys. *International Journal of Marine Energy*, **12**, 63–76.

838 Longuet-Higgins, M. S., 1986: Eulerian and Lagrangian aspects of surface waves. *J. Fluid Mech.*,
839 **173**, 683–707.

840 Longuet-Higgins, M. S., and R. Stewart, 1962: Radiation stress and mass transport in gravity
841 waves, with applications to 'surf beats'. *J. Fluid Mech.*, **13**, 481–504.

842 Longuet-Higgins, M. S., and R. W. Stewart, 1964: Radiation stresses in water waves; a physical
843 discussion, with applications. *Deep-Sea Res.*, **2**, 529–562.

844 Marthinsen, T., and S. R. Winterstein, 1992: On the skewness of random surface waves. *The*
845 *Second International Offshore and Polar Engineering Conference*.

McAllister, M. L., T. A. A. Adcock, P. H. Taylor, and T. S. van den Bremer, 2018: The set-down and set-up of directionally spread and crossing surface gravity wave groups. *J. Fluid Mech.*, **835**, 131–169.

Meylan, M. H., L. J. Yiew, L. G. Bennetts, B. J. French, and G. A. Thomas, 2015: Surge motion of an ice floe in waves: comparison of a theoretical and an experimental model. *Ann. Glaciol.*, **56**, 155–159.

Mork, G., S. Barstow, A. Kabuth, and M. T. Pontes, 2010: Assessing the global wave energy potential. *ASME 2010 29th International conference on ocean, offshore and arctic engineering*, 447–454.

Okihiro, M., R. T. Guza, and R. J. Seymour, 1992: Bound infra-gravity waves. *J. Geophys. Res.*, **97**, 453–469.

O'Reilly, W. C., T. H. C. Herbers, R. J. Seymour, and R. T. Guza, 1996: A comparison of directional buoy and fixed platform measurements of Pacific swell. *J. Atmospheric Ocean. Technol.*, **13**, 231–238.

Pellet, L., P. Christodoulides, S. Donne, C. J. Bean, and F. Dias, 2017: Pressure induced by the interaction of water waves with nearly equal frequencies and nearly opposite directions. *Theoretical and Applied Mechanics Letters*.

Penny, W. G., and A. T. Price, 1952: Part ii. Finite periodic stationary gravity waves in a perfect liquid. *Philos. Trans. Royal Soc. Lon. A*, **244**, 254–284.

Phillips, O. M., D. Gu, and M. Donelan, 1993: Expected structure of extreme waves in a Gaussian sea. Part i: Theory and SWADE buoy measurements. *J. Phys. Oceanogr.*, **23**, 992–1000.

867 Pizzo, N., W. K. Melville, and L. Deike, 2019: Lagrangian transport by nonbreaking and breaking
868 deep-water waves at the ocean surface. *J. Phys. Oceanogr.*, **49**, 983–992.

869 Pontes, M. T., 1998: Assessing the European wave energy resource. *J. Offshore Mech. Arct.*, **120**,
870 226–231.

871 Prevosto, M., H. E. Krogstad, and R. Agnès, 2000: Probability distributions for maximum wave
872 and crest heights. *Coastal Engineering*, **40**, 329–360.

873 Rademakers, P. J., 1993: Waverider-wavestaff comparison. *Ocean Eng*, **20**, 187–193.

874 Raghukumar, K., G. Chang, F. Spada, C. Jones, T. Janssen, and A. Gans, 2019: Performance char-
875 acteristics of "Spotter", a newly developed real-time wave measurement buoy. *J. Atmospheric*
876 *Ocean. Technol.*, **36**.

877 Rayleigh, L., 1915: Deep water waves, progressive or stationary, to the third order of approxima-
878 tion. *Proc. R. Soc. Lon. A*, **91**, 345–353.

879 Santamaria, F., G. Boffetta, M. M. Afonso, A. Mazzino, M. Onorato, and D. Pugliese, 2013:
880 Stokes drift for inertial particles transported by water waves. *EPL (Europhysics Letters)*, **102**,
881 14 003.

882 Santo, H., P. H. Taylor, R. Eatock Taylor, and Y. S. Choo, 2013: Average properties of the largest
883 waves in Hurricane Camille. *J. Offshore Mech. Arct.*, **135**, 011 602.

884 Sharma, J. N., and R. G. Dean, 1981: Second-order directional seas and associated wave forces.
885 *Soc. Petrol. Eng. J.*, **21**, 129–140.

886 Soares, C. G., Z. Cherneva, and E. M. Antao, 2004: Steepness and asymmetry of the largest waves
887 in storm sea states. *Ocean Eng.*, **31**, 1147–1167.

888 Srokosz, M. A., and M. S. Longuet-Higgins, 1986: On the skewness of sea-surface elevation. *J.*
889 *Fluid Mech.*, **164**, 487–497.

890 Stokes, G. G., 1847: On the theory of oscillatory waves. *Trans. Camb. Philos. Soc.*, **8**, 441–455.

891 Tadjbakhsh, I., and J. B. Keller, 1960: Standing surface waves of finite amplitude. *J. Fluid Mech.*,
892 **8**, 442451.

893 Toffoli, A., J. Monbaliu, M. Onorato, A. R. Osborne, A. V. Babanin, and E. M. Bitner-Gregersen,
894 2007: Second-order theory and setup in surface gravity waves: a comparison with experimental
895 data. *J. Phys. Oceanogr.*, **37**, 2726–2739.

896 Toffoli, A., M. Onorato, and J. Monbaliu, 2006: Wave statistics in unimodal and bimodal seas
897 from a second-order model. *Eur. J. Mech. B-Fluid.*, **25 (5)**, 649–661.

898 Van Essen, S., K. Ewans, and J. McConichie, 2018: Wave buoy performance in short and long
899 waves, evaluated using tests on a hexapod. *ASME 2018 37th International Conference on*
900 *Ocean, Offshore and Arctic Engineering*.

901 Walker, D. A. G., P. H. Taylor, and R. Eatock Taylor, 2004: The shape of large surface waves on
902 the open sea and the Draupner New Year wave. *App. Ocean Res.*, **26**, 73–83.

903 Waseda, T., and Coauthors, 2014: Deep water observations of extreme waves with moored and
904 free GPS buoys. *Ocean Dynamics*, **64**, 1269–1280.

905 Whittaker, C. N., A. C. Raby, C. J. Fitzgerald, and P. H. Taylor, 2016: The average shape of large
906 waves in the coastal zone. *Coast. Eng.*, **114**, 253–264.

LIST OF TABLES

Table 1. Approximate second-order Eulerian and Lagrangian free surface elevations and frequencies for foccused wave groups at the point of focus. The surface elevations are given in non-dimensional form $\tilde{\eta}^{(2)} = \eta^{(2)}(x=0,y=0)/(k_0 a_0^2/2)$ with $\varphi_0 = -\omega_0 t + \mu_0$, $R = \sigma_x/\sigma_y$, $+$ and $-$ denoting super- and subharmonic contributions, respectively, and a_0 the linearly focussed amplitude of the envelope at $(x=0,y=0)$. The function $F(k_0 d, \sigma_\theta)$ is defined in (43) and lies between 0 ($\sigma_\theta = 0$) and -1.31 ($\sigma_\theta \to \infty$) for $k_0 d \to \infty$. The Eulerian subharmonic set-down for the weakly spread group is evaluated at the time of focus $t = 0$. The steepness is denoted by $\alpha = k_0 a_0$. 48

Table 2. Experimental matrix († represents experiments carried out without auxiliary mooring). 49

Table 3. Input and estimated spectral parameters, where the estimated spectral parameters are denoted by a $\star$, a † represents tests which were repeated 3 times and a - tests which were omitted (black rectangles are an artefact of compiling in single column mode). 50

Table 4. Quantification of errors associated with repeatability (error measure I). 51

TABLE 1. Approximate second-order Eulerian and Lagrangian free surface elevations and frequencies for foccused wave groups at the point of focus. The surface elevations are given in non-dimensional form $\tilde{\eta}^{(2)} = \eta^{(2)}(x=0,y=0)/(k_0 a_0^2/2)$ with $\varphi_0 = -\omega_0 t + \mu_0$, $R = \sigma_x/\sigma_y$, $+$ and $-$ denoting super- and subharmonic contributions, respectively, and a_0 the linearly focussed amplitude of the envelope at $(x=0,y=0)$. The function $F(k_0 d, \sigma_\theta)$ is defined in (43) and lies between 0 ($\sigma_\theta = 0$) and -1.31 ($\sigma_\theta \to \infty$) for $k_0 d \to \infty$. The Eulerian subharmonic set-down for the weakly spread group is evaluated at the time of focus $t = 0$. The steepness is denoted by $\alpha = k_0 a_0$.

		Weakly spread group (WSG)	Crossing groups (CWGs)	Strongly spread group (SSG)
			$(A_1(X_1=0,Y_1=0) = A_2(X_2=0,Y_2=0) = a_0/2)$	
Eulerian surface elevation $\tilde{\eta}_{\mathrm{E}}^{(2)}$	+	$\cos(2\varphi_0)$	$\frac{1}{4}\cos(2\varphi_1) + \frac{1}{4}\cos(2\varphi_2)$ $+\left(\frac{1}{4}(3-\cos(\Delta\theta)) - \frac{2(1-\cos(\Delta\theta))}{4-\sqrt{2+2\cos(\Delta\theta)}}\right)\cos(\varphi_1+\varphi_2)$	$\left(\frac{3}{2} + F(k_0 d,\sigma_\theta) - \frac{1}{2}e^{-\sigma_\theta^2}\right)\cos(2\varphi_0)$
	-	$-\frac{1}{2k_0 d(1+R)}$	$\tilde{\eta}_{\mathrm{E,SD}}^{(2)} + \frac{1}{4}(1-\cos(\Delta\theta))\cos(\varphi_1-\varphi_2)$	$\tilde{\eta}_{\mathrm{E,SD}}^{(2)} + \frac{1}{2}\left(1-e^{-\sigma_\theta^2}\right)$
Lagrangian correction to surface elevation $\Delta\tilde{\eta}_{\mathrm{L}}^{(2)}$	+	$-\cos(2\varphi_0)$	$-\frac{1}{4}\cos(2\varphi_1)) - \frac{1}{4}\cos(2\varphi_2)) - \frac{1}{2}\cos(\Delta\theta)\cos(\varphi_1+\varphi_2)$	$-e^{-\sigma_\theta^2}\cos(2\varphi_0)$
	-	1	$\frac{1}{2} + \frac{1}{2}\cos(\Delta\theta)\cos(\varphi_1-\varphi_2)$	$e^{-\sigma_\theta^2}$
Lagrangian surface elevation $\tilde{\eta}_{\mathrm{L}}^{(2)}$	+	0	$(1-\cos(\Delta\theta))\left(\frac{3}{4} - \frac{2}{4-\sqrt{2+2\cos(\Delta\theta)}}\right)\cos(\varphi_1+\varphi_2)$	$\left(\frac{3}{2} + F(k_0 d,\sigma_\theta) - \frac{3}{2}e^{-\sigma_\theta^2}\right)\cos(2\varphi_0)$
	-	$1-\frac{1}{2k_0 d(1+R)}$	$\tilde{\eta}_{\mathrm{E,SD}}^{(2)} + \frac{1}{2} + \frac{1}{4}(1+\cos(\Delta\theta))\cos(\varphi_1-\varphi_2)$	$\tilde{\eta}_{\mathrm{E,SD}}^{(2)} + \frac{1}{2}\left(1+e^{-\sigma_\theta^2}\right)$
Lagrangian frequency $\frac{\omega_{\mathrm{L},0}}{\omega_0}$		$1-\alpha^2$	$1 - \frac{1}{4}\alpha^2\left((1+\cos(\Delta\theta)) + 2\cos^4(\Delta\theta/2)\right)$	$1 - \frac{\alpha^2}{4}\left(3e^{-\sigma_\theta^2/2} + e^{-5\sigma_\theta^2/2}\right)$

TABLE 2. Experimental matrix († represents experiments carried out without auxiliary mooring).

Category	D (m)	a_0 (m)	σ_θ (.deg)	$\Delta\theta$ (.deg)
Spreading	0.07	0.15	0,10, 20†, 30, 40†, 50, $\infty^\dagger$	0
	0.07	0.20	20, 40, ∞	0
Crossing	0.07	0.15	20	45, 90, 135, 180

TABLE 3. Input and estimated spectral parameters, where the estimated spectral parameters are denoted by a $\star$, a † represents tests which were repeated 3 times and a - tests which were omitted (black rectangles are an artefact of compiling in single column mode).

	Input					Eulerian				Lagrangian			
Test no.	σ_θ (.deg)	$\Delta\theta$ (.deg)	ω_0 (rad/s)	a_0 (m)	Δk (m^{-1})	$\sigma^\star_\theta$ (.deg)	$\omega^\star_{E,0}$ (rad/s)	$a^\star_{E,0}$ (m)	$\Delta\omega^\star_E$ (rad/s)	$\omega^\star_{L,0}$ (rad/s)	$a^\star_{L,0}$ (m)	$\Delta\omega^\star_L$ (rad/s)
1.1	0	0	4.4	0.3	0.6	0	4.19	0.157	1.18	4.05	0.159	1.17
1.2	10	0	4.4	0.3	0.6	7.8	4.18	0.137	1.11	4.08	0.137	1.10
1.3†	20	0	4.4	0.3	0.6	15.7	4.18	0.123	1.05	4.10	0.121	0.99
1.4	30	0	4.4	0.3	0.6	28.0	4.25	0.127	1.07	4.17	0.134	1.10
1.5†	40	0	4.4	0.3	0.6	38.0	4.25	0.127	1.08	4.19	0.134	1.10
1.6	50	0	4.4	0.3	0.6	47.6	4.25	0.126	1.06	4.20	0.13	1.09
1.7†	∞	0	4.4	0.3	0.6	-	-	-	-	4.24	0.121	0.62
2.1	0	0	4.4	0.4	0.6	0	3.98	0.206	1.37	3.89	0.212	1.48
2.2	20	0	4.4	0.4	0.6	17.6	4.13	0.165	1.17	4.00	0.165	1.21
2.3	40	0	4.4	0.4	0.6	38.6	4.25	0.168	1.08	4.14	0.176	1.08
2.4	∞	0	4.4	0.4	0.6	∞	4.24	0.169	1.04	4.24	0.170	1.08
3.1	20	45	4.4	0.3	0.6	17.8	4.25	0.129	1.09	4.17	0.133	1.02
3.2	20	90	4.4	0.3	0.6	18.6	4.25	0.129	1.09	4.21	0.133	1.02
3.3	20	135	4.4	0.3	0.6	19.1	4.23	0.131	1.09	4.23	0.134	1.00
3.4	20	180	4.4	0.3	0.6	18.6	4.24	0.130	1.04	4.24	0.136	1.01

Description	Test parameters	Error	
		$\pm\Delta\eta_{-}^{(2)}$ (mm)	$\pm\Delta\eta_{+}^{(2)}$ (mm)
Two standard deviations of the	$\sigma_\theta = 20^\circ$	0.20	1.00
measured wave-averaged surface	$\sigma_\theta = 40^\circ$	0.08	0.22
amplitude $a_M^{(2)}$ from repeats	$\sigma_\theta \to \infty$	0.09	0.32

TABLE 4. Quantification of errors associated with repeatability (error measure I).

LIST OF FIGURES

Fig. 1. Comparison of our approximate expressions (dotted lines with solid circles for clarity) to exact multi-chromatic (solid lines) second-order sub- (left column), super-harmonic (middle column) bound wave components and their sum (right column), for directionally spread (a-c) and crossing (d-f) focused wave groups based on narrow Gaussian spectra (spectral width $\Delta k = 0.1$ m^{-1}) on a water depth $d = 2$ m, with peak wavenumber $k_0 = 1.97$ m^{-1} and for focussed crests ($\mu_0 = \mu_1 = \mu_2 = 0$). The red, grey and blue lines respectively denote the magnitude $\tilde{a}^{(2)} = a^{(2)}/(k_0 a_0^2/2)$ of the Eulerian components $\eta_{\mathrm{E}}^{(2)}$, the Lagrangian corrections $\Delta\eta_{\mathrm{L}}^{(2)}$ and the Lagrangian components $\eta_{\mathrm{L}}^{(2)}$. Open circles are used in panels c and f for visual clarity. 54

Fig. 2. Amplitude of Eulerian (red) and Lagrangian (blue) second-order bound wave components from exact multi-chromatic second-order theory for crossing focused wave groups with Gaussian ($\Delta k = 0.6$ m^{-1}, representative of our experiments) and JONSWAP spectra ($\gamma = 3.3$, $n = -5$), as shown by solid and dashed lines, respectively. The groups have input degrees of directional spreading of $\sigma_\theta = 20^\circ$, peak frequencies of 0.7 Hz, and a depth of 2.0 m ($k_0 d = 3.9$). The dot-dashed lines show predictions using exact multi-chromatic second-order theory for a JONSWAP spectrum with an increased depth of $d = 4.0$ m. Dotted lines show predictions using our narrow-banded approximations. Panels a, b, and c plot the amplitude of sub-, super-, and total bound wave components as a function of the crossing angle $\Delta\theta$. 55

Fig. 3. Eulerian (black lines) and Lagrangian (red dashed lines) linear free surface elevation $\eta^{(1)}$ for a weakly spread group (WSG, $\sigma_\theta = 20^\circ$, panel a) and a strongly spread group (SSG, $\sigma_\theta \to \infty$, panel b) and their amplitude spectra $\hat{\eta}^{(1)}$ (panels c and d, respectively) for steepness $a_0 k_0 = 0.4$. The Lagrangian peak frequency $\omega_{\mathrm{L},0}$ is calculated using (48), noting that we obtain $\omega_{\mathrm{L},0} \to \omega_0$ for $\sigma_\theta \to \infty$. 56

Fig. 4. Measured wave crest amplitude for directionally spread wave groups with input steepness $a_0 k_0 = 0.3$ (circles) and $a_0 k_0 = 0.4$ (triangles) and crossing wave groups ($a_0 k_0 = 0.3$, crosses). Panel a compares the crest amplitude a_{L} measured by our Lagrangian buoy to Eulerian measurements a_{E} with red markers showing fully non-linear measured crest amplitudes and black markers showing linearised crest heights. Panel b shows how the ratio of linearized amplitudes $a_{\mathrm{L}}^{(1)}/a_{\mathrm{E}}^{(1)}$ varies as a function of directional spreading and crossing angle. 57

Fig. 5. Second-order bound wave components for weakly and strongly spread wave groups with input degrees of directional spreading $\sigma_\theta = 0 - 50^\circ$ in increments of 10° and input steepness $a_0 k_0 = 0.3$. Estimated degrees of directional spreading $\sigma_\theta^\star$ are given in the figure. The top row (panels a to f) shows sub-harmonic bound wave components, and the bottom row (panels g to l) shows super-harmonic bound wave components. In all panels black solid lines show Eulerian measurements, and black dot-dashed lines show Lagrangian measurements. Red dashed lines and blue dotted lines show predictions made using Eulerian and Lagrangian second-order theory, respectively. Grey envelopes show measurement error bounds. 58

Fig. 6. Second-order bound wave components for two crossing wave groups with input degrees of directional spreading $\sigma_\theta = 20^\circ$, input steepness $a_0 k_0 = 0.3$, and crossing angle between the two wave groups $\Delta\theta = 45, 90, 135$ and 180°. Estimated degrees of directional spreading $\sigma_\theta^\star$ are given in the figure. The top row (panels a to d) shows sub-harmonic bound wave components, and the bottom row (panels e to h) shows super-harmonic bound wave components. In all panels, black solid lines show Eulerian measurements, and black dot-dashed

lines show Lagrangian measurements. Red dashed lines and blue dotted lines show predictions made using Eulerian and Lagrangian second-order theory, respectively. Grey envelopes show measurement error bounds. 59

Fig. 7. Amplitudes of Eulerian and Lagrangian second-order bound wave components for weakly and strongly directionally spread focused wave groups. Panel a compares theoretical predictions (T) to the measured (M) amplitude of both super- and sub-harmonic components (crosses and circles, respectively). Panels b, c, and d plot the amplitude of sub-, super-, and total bound wave components as a function of the estimated degree of directional spreading $\sigma_\theta^\star$. Throughout, blue markers represent Lagrangian measurements and black represent Eulerian measurements. Similarly, the blue and red dashed lines represent theoretical Lagrangian and Eulerian predictions, respectively. 60

Fig. 8. Amplitudes of Eulerian and Lagrangian second-order bound wave components for two crossing focused wave groups with input degrees of directional spreading $\sigma_\theta = 20^\circ$. Panel a compares theoretical predictions (T) to the measured (M) amplitudes of both super- and sub-harmonic components (crosses and circles, respectively)). Panels b, c, and d plot the amplitude of sub-, super-, and total bound wave components as a function of the crossing angle $\Delta\theta$. Throughout, blue markers represent Lagrangian measurements and black represent Eulerian measurements. Similarly, the blue and red dashed lines represent theoretical Lagrangian and Eulerian predictions, respectively. 61

Fig. 9. Comparison of total measured Eulerian (black lines) and Lagrangian (red dashed lines) free surface elevations for weakly and strongly spread wave groups (WSG and SSG, respectively) of input steepness $a_0k_0 = 0.4$. 62

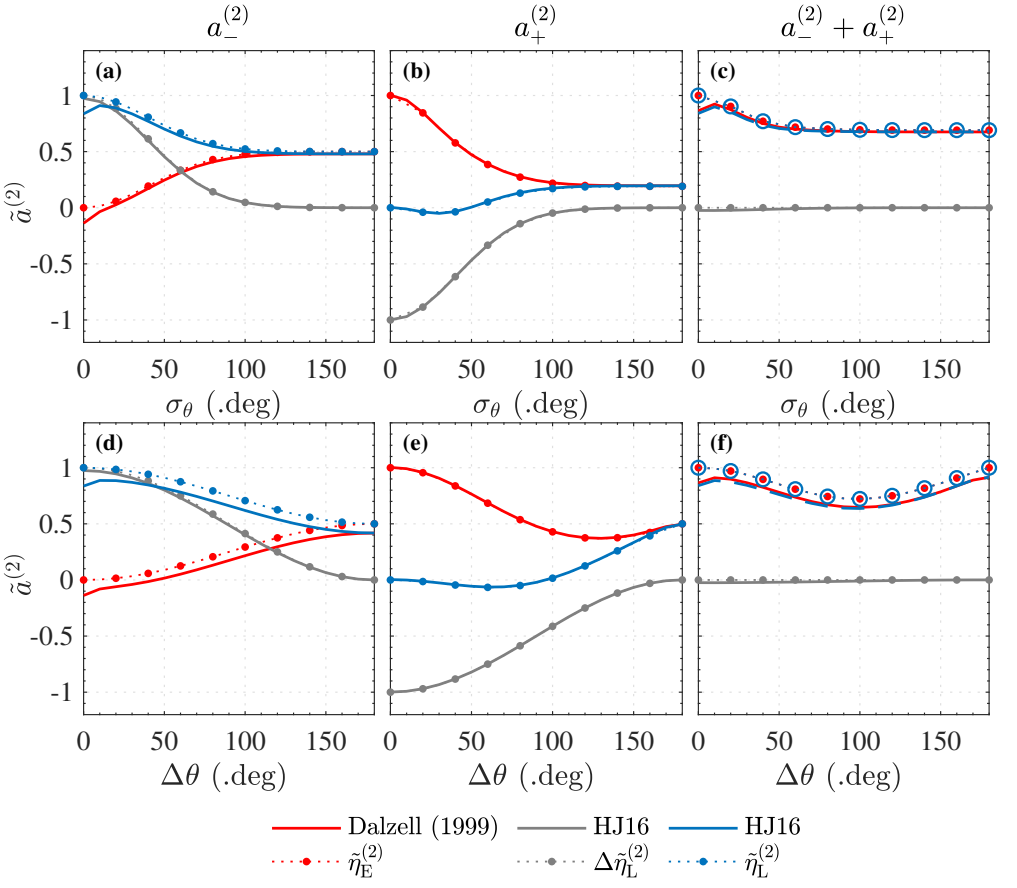

FIG. 1. Comparison of our approximate expressions (dotted lines with solid circles for clarity) to exact multi-chromatic (solid lines) second-order sub- (left column), super-harmonic (middle column) bound wave components and their sum (right column), for directionally spread (a-c) and crossing (d-f) focused wave groups based on narrow Gaussian spectra (spectral width $\Delta k = 0.1$ m^{-1}) on a water depth $d = 2$ m, with peak wavenumber $k_0 = 1.97$ m^{-1} and for focussed crests ($\mu_0 = \mu_1 = \mu_2 = 0$). The red, grey and blue lines respectively denote the magnitude $\tilde{a}^{(2)} = a^{(2)}/(k_0 a_0^2/2)$ of the Eulerian components $\eta_{\mathrm{E}}^{(2)}$, the Lagrangian corrections $\Delta\eta_{\mathrm{L}}^{(2)}$ and the Lagrangian components $\eta_{\mathrm{L}}^{(2)}$. Open circles are used in panels c and f for visual clarity.

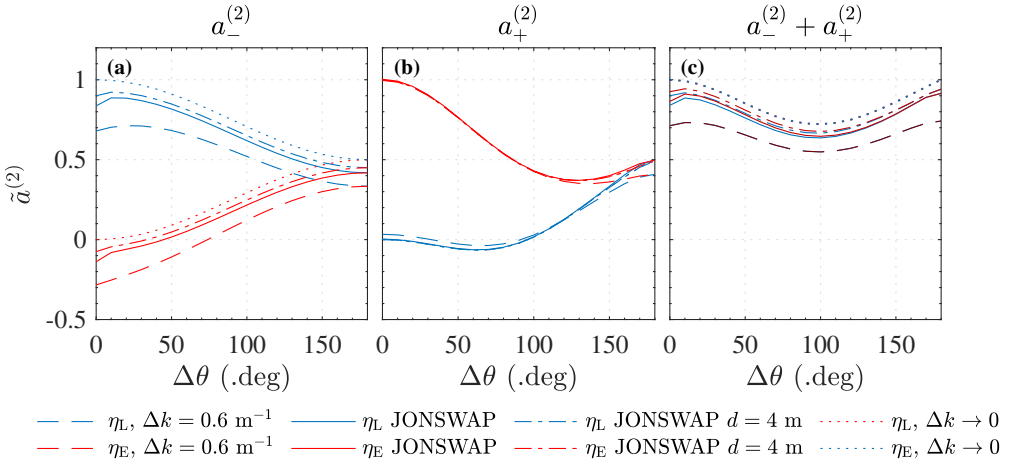

FIG. 2. Amplitude of Eulerian (red) and Lagrangian (blue) second-order bound wave components from exact multi-chromatic second-order theory for crossing focused wave groups with Gaussian ($\Delta k = 0.6$ m^{-1}, representative of our experiments) and JONSWAP spectra ($\gamma = 3.3$, $n = -5$), as shown by solid and dashed lines, respectively. The groups have input degrees of directional spreading of $\sigma_\theta = 20°$, peak frequencies of 0.7 Hz, and a depth of 2.0 m ($k_0 d = 3.9$). The dot-dashed lines show predictions using exact multi-chromatic second-order theory for a JONSWAP spectrum with an increased depth of $d = 4.0$ m. Dotted lines show predictions using our narrow-banded approximations. Panels a, b, and c plot the amplitude of sub-, super-, and total bound wave components as a function of the crossing angle $\Delta\theta$.

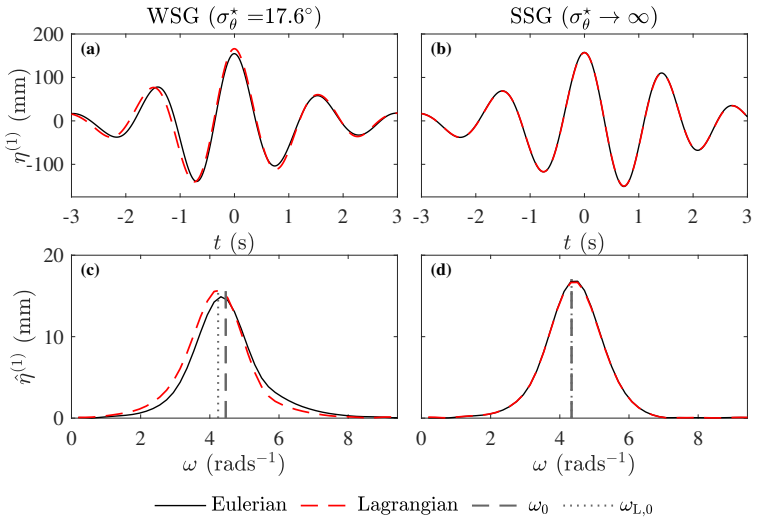

FIG. 3. Eulerian (black lines) and Lagrangian (red dashed lines) linear free surface elevation $\eta^{(1)}$ for a weakly spread group (WSG, $\sigma_\theta = 20°$, panel a) and a strongly spread group (SSG, $\sigma_\theta \to \infty$, panel b) and their amplitude spectra $\hat{\eta}^{(1)}$ (panels c and d, respectively) for steepness $a_0 k_0 = 0.4$. The Lagrangian peak frequency $\omega_{L,0}$ is calculated using (48), noting that we obtain $\omega_{L,0} \to \omega_0$ for $\sigma_\theta \to \infty$.

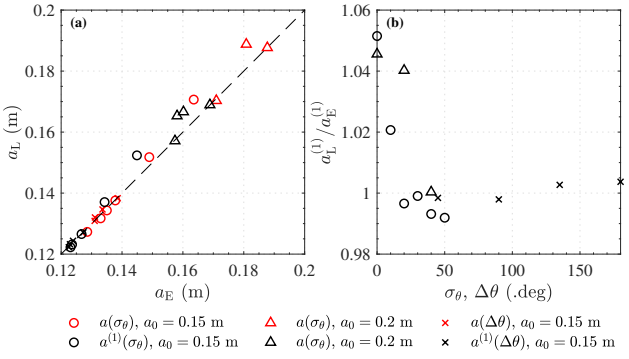

FIG. 4. Measured wave crest amplitude for directionally spread wave groups with input steepness $a_0k_0 = 0.3$ (circles) and $a_0k_0 = 0.4$ (triangles) and crossing wave groups ($a_0k_0 = 0.3$, crosses). Panel a compares the crest amplitude a_{L} measured by our Lagrangian buoy to Eulerian measurements a_{E} with red markers showing fully non-linear measured crest amplitudes and black markers showing linearised crest heights. Panel b shows how the ratio of linearized amplitudes $a_{\mathrm{L}}^{(1)}/a_{\mathrm{E}}^{(1)}$ varies as a function of directional spreading and crossing angle.

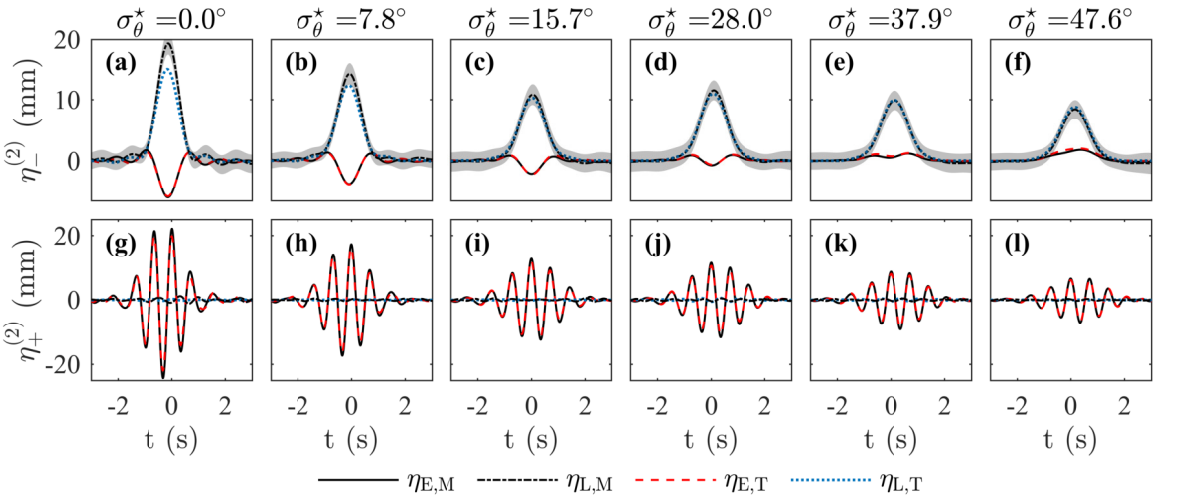

FIG. 5. Second-order bound wave components for weakly and strongly spread wave groups with input degrees of directional spreading $\sigma_\theta = 0 - 50°$ in increments of 10° and input steepness $a_0 k_0 = 0.3$. Estimated degrees of directional spreading $\sigma_\theta^\star$ are given in the figure. The top row (panels a to f) shows sub-harmonic bound wave components, and the bottom row (panels g to l) shows super-harmonic bound wave components. In all panels black solid lines show Eulerian measurements, and black dot-dashed lines show Lagrangian measurements. Red dashed lines and blue dotted lines show predictions made using Eulerian and Lagrangian second-order theory, respectively. Grey envelopes show measurement error bounds.

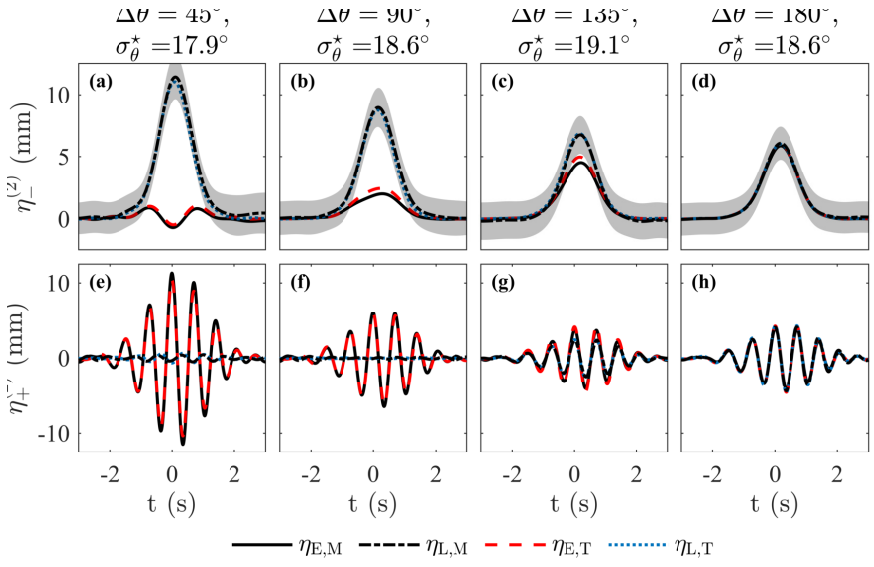

FIG. 6. Second-order bound wave components for two crossing wave groups with input degrees of directional spreading $\sigma_\theta = 20°$, input steepness $a_0 k_0 = 0.3$, and crossing angle between the two wave groups $\Delta\theta = 45, 90, 135$ and $180°$. Estimated degrees of directional spreading $\sigma^\star_\theta$ are given in the figure. The top row (panels a to d) shows sub-harmonic bound wave components, and the bottom row (panels e to h) shows super-harmonic bound wave components. In all panels, black solid lines show Eulerian measurements, and black dot-dashed lines show Lagrangian measurements. Red dashed lines and blue dotted lines show predictions made using Eulerian and Lagrangian second-order theory, respectively. Grey envelopes show measurement error bounds.

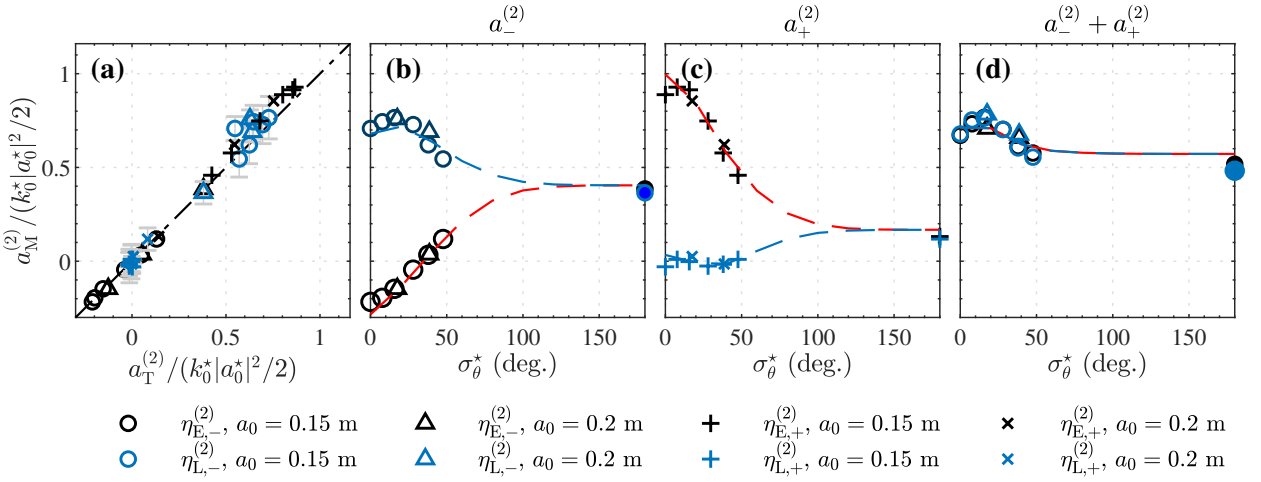

FIG. 7. Amplitudes of Eulerian and Lagrangian second-order bound wave components for weakly and strongly directionally spread focused wave groups. Panel a compares theoretical predictions (T) to the measured (M) amplitude of both super- and sub-harmonic components (crosses and circles, respectively). Panels b, c, and d plot the amplitude of sub-, super-, and total bound wave components as a function of the estimated degree of directional spreading $\sigma_\theta^\star$. Throughout, blue markers represent Lagrangian measurements and black represent Eulerian measurements. Similarly, the blue and red dashed lines represent theoretical Lagrangian and Eulerian predictions, respectively.

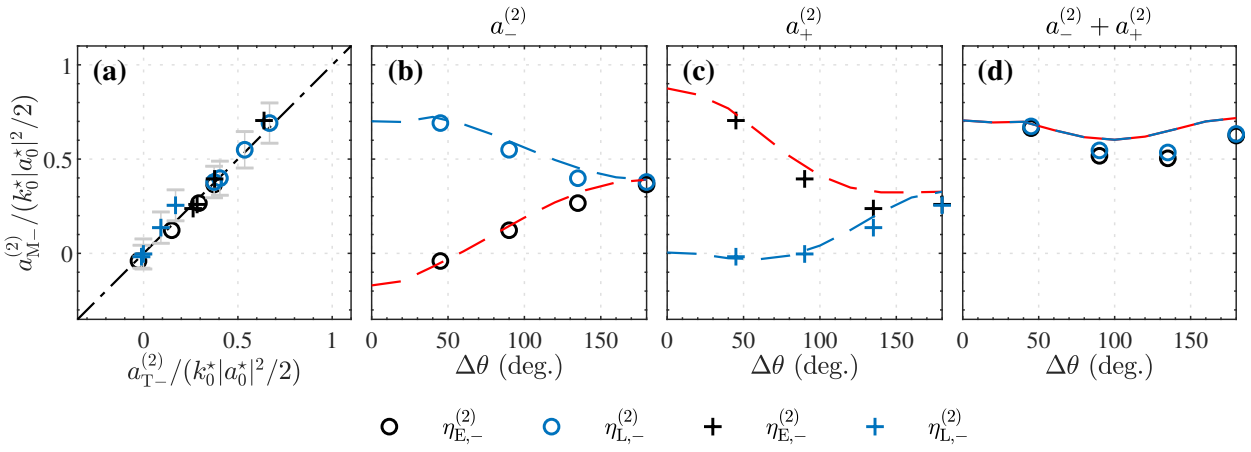

FIG. 8. Amplitudes of Eulerian and Lagrangian second-order bound wave components for two crossing focused wave groups with input degrees of directional spreading $\sigma_\theta = 20°$. Panel a compares theoretical predictions (T) to the measured (M) amplitudes of both super- and sub-harmonic components (crosses and circles, respectively)). Panels b, c, and d plot the amplitude of sub-, super-, and total bound wave components as a function of the crossing angle $\Delta\theta$. Throughout, blue markers represent Lagrangian measurements and black represent Eulerian measurements. Similarly, the blue and red dashed lines represent theoretical Lagrangian and Eulerian predictions, respectively.

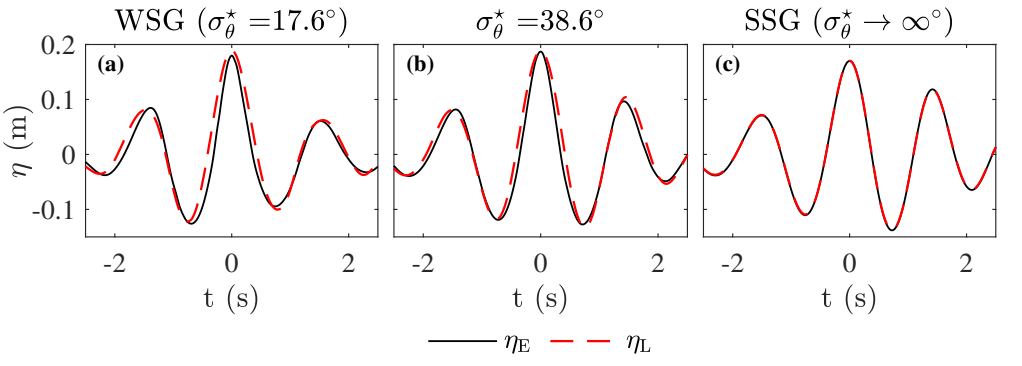

FIG. 9. Comparison of total measured Eulerian (black lines) and Lagrangian (red dashed lines) free surface elevations for weakly and strongly spread wave groups (WSG and SSG, respectively) of input steepness $a_0 k_0 = 0.4$.